ORIGINAL ARTICLE

Intensity-Curvature Measurement Approaches for the Diagnosis of Magnetic Resonance Imaging Brain Tumors

Carlo Ciulla [a],*, **Dimitar Veljanovski** [b], **Ustijana Rechkoska Shikoska** [a], **Filip A. Risteski** [b]

[a] *University for Information Science & Technology, Partizanska B.B., 6000 Ohrid, Macedonia*
[b] *Skopje City General Hospital, Pariska B.B., 1000 Skopje, Macedonia*

A B S T R A C T

This research presents signal-image post-processing techniques called Intensity-Curvature Measurement Approaches with application to the diagnosis of human brain tumors detected through Magnetic Resonance Imaging (MRI). Post-processing of the MRI of the human brain encompasses the following model functions: (i) bivariate cubic polynomial, (ii) bivariate cubic Lagrange polynomial, (iii) monovariate sinc, and (iv) bivariate linear. The following Intensity-Curvature Measurement Approaches were used: (i) classic-curvature, (ii) signal resilient to interpolation, (iii) intensity-curvature measure and (iv) intensity-curvature functional. The results revealed that the classic-curvature, the signal resilient to interpolation and the intensity-curvature functional are able to add additional information useful to the diagnosis carried out with MRI. The contribution to the MRI diagnosis of our study are: (i) the enhanced gray level scale of the tumor mass and the well-behaved representation of the tumor provided through the signal resilient to interpolation, and (ii) the *visually perceptible* third dimension perpendicular to the image plane provided through the classic-curvature and the intensity-curvature functional.

© 2015 Production and hosting by Elsevier B.V. on behalf of Cairo University.

* Corresponding author. Tel.: +389 46 511 585; fax: +389 46 511 567.
E-mail addresses: cxc2728@njit.edu, carlo.ciulla@uist.edu.mk (C. Ciulla).

Introduction

The organization of the manuscript

The manuscript is organized as follows. The literature is addressed thoroughly in the introduction and discussion sections so as to relate it to the main research topic of the paper which is that one of proposing post-processing techniques (Intensity-Curvature Measurement Approaches) in order to collect from MRI complementary and/or additional
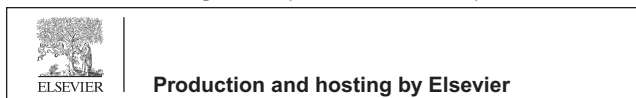
information of the human brain tumor, and so to aid the diagnosis of the tumor. The mathematical formulation of the Intensity-Curvature Measurement Approaches is placed in the manuscript in the methodology section. The results are presented through images resulting from the Intensity-Curvature Measurement Approaches. There is immediate correlation between: (i) the concepts (Intensity-Curvature Measurement Approaches) treated by the paper in theoretical form (through the formulae given in the section titled: 'The mathematical formulation'), and (ii) the results presented through the images obtained from the application of the concepts. The discussion section places the emphasis on the significance of the results. The conclusion section is a stand alone paragraph which conveys to the reader what the paper reports.

The motivation of the literature review

The review of related work is preparatory to the statement of the working hypothesis which is given in the subsection titled: 'The contribution of the present works'. Therefore, the category of the literature reviewed is the one that focuses on MRI derived techniques which provide complementary and/or additional information to T1-weighted MRI. For instance, T2-weighted MRI is of help in the visualization of the human brain fat and water, which, if imaged with T1-weighted MRI, would not be seen as clearly when using T2-weighted MRI. Another example of collection of complementary and/or additional information is the use of the contrast agent in T1-weighted MRI. Thus, the paper reviews the literature while searching for evidence of MRI techniques based collectible information which is capable of complementing and adding to the information collected with T1-weighted MRI. Advantages, disadvantages and motivations to the use of the various and different MRI techniques are already known in the literature. Comparison between MRI techniques is beyond the scope of this manuscript. The scope of the present works is to present the signal-image post-processing techniques called Intensity-Curvature Measurement Approaches and to frame the techniques into the scientific literature as valuable methodology employable to collect complementary and/or additional information from T1-weighted MRI, T2-weighted MRI and Fluid Attenuated Inversion Recovery (FLAIR) imaging modalities.

The literature

Human brain tumor detection through the use of Magnetic Resonance Imaging (MRI) is a widespread technique for the diagnosis. MRI provides the information related to the anatomy of the pathology and such information is used in order to classify the tumor. The tumor embeds in its structure the key to the correct diagnosis and moreover embeds details that can be enhanced through the post-processing of the MRI images [1–3].

Human brain tumor detection can be performed and disease progression can be monitored by a variety of MR techniques [4] among which are here recalled: Diffusion Weighted Imaging (DWI), Diffusion Tensor Imaging (DTI), Proton MR Spectroscopic Imaging (MRS), Perfusion MR Imaging (PWI), and Dynamic Susceptibility Weighted Contrast-Enhanced (DSC) MR Imaging. However, enhanced T1-weighted Imaging is the most useful diagnostic technique

and also the most used to monitor the progression (regression) of the disease [4]. Additionally, MR Imaging techniques have progressed to the level of being able to monitor molecule movements, the microvascular integrity and hemodynamic characteristics, and the chemical characteristics of some chemical compounds [5].

The literature reports a wide array of MR applications to the study and the diagnosis of human brain tumors. Distinction between radiation necrosis and brain metastasis was achieved with PET co-registered to MRI [6]. Another approach to the study of the human brain tumor is the one that makes use of T2-weighted images and maps of absolute regional cerebral blood flow (rCBF) derived from arterial spin labeling (ASL) [7]. The capability to make an accurate diagnosis of abscesses and cystic/necrotic brain tumors using Diffusion Weighted Imaging has been studied through research which made use of T1-weighted and T2-weighted MRI [8]. Within the context of the study of the assessment of an improved diagnosis of cerebral gliomas a study [9] reports the use of PET and MRI used with co-registration. Also, a recent study [10] used pre-contrast and post-contrast Susceptibility Weighted Imaging (SWI) in order to assess the diagnosis of brain neoplasms. Another study reports findings subsequent to the Magnetic Resonance Spectroscopy (MRS) study of a brain hemangioblastoma [11].

The literature shows that MRS is a source of additional information to the one collected through the use of T1-weighted MRI [12]. The information collected through MRS is on tumor malignancy and characteristic tumor metabolism [12]. However, it was argued that proton MRS alone is not comparable to MRI in the diagnosis of the brain tumor and thus it was proposed that pattern recognition of the biochemical information obtained with proton MRS can make an accurate diagnosis of the tumor [13]. As far as regards the use of computer based techniques for tumor type classification and grading is concerned, a study which uses pattern classification of data obtained through MRI and perfusion MRI was used and proved useful to the diagnosis of the tumor [14].

The use of contrast-enhanced computed tomography (CCT) for the diagnosis of brain metastases was investigated in comparison with MRI and the findings were in favor of the accuracy of the diagnosis through the use of MRI [15]. Another approach uses a comparison of MRI with Diffusion Weighted Imaging (DWI) while studying brain abscess and cystic or necrotic brain tumors, and finds that DWI, specifically to the results reported in the study, performs better than T1-weighted imaging [16]. T1-weighted imaging was also used in order to detect brain tumors and/or affections of the vascular system [17]. Insights into tumor pathogenesis were collected during a study that uses cancer stem cell (CSC) in mouse brains [18]. In order to assess both tumor cellularity and the grading of the gliomas, a study reports on a technique based on the use of diffusion-weighted Magnetic Resonance Imaging with echo-planar imaging (EPI) [19], which proves useful to the diagnosis and the characteristics of the gliomas. MRI has also been proven useful to fetal MRI [20].

The contribution of the present works

Recent studies have employed post-processing techniques in order to gain information from the human brain tumor MRI

[1–3]. The post-processing techniques of the MRI images, which are proposed in this paper, are based on Intensity-Curvature Measurement Approaches. The intensity is the value of the MRI signal, whereas the curvature is the sum of all of the second order derivatives of the Hessian of the polynomial function fitted to the MRI data. The steps followed in order to collect information from the MRI images are: (i) fitting a model function to the data, (ii) re-sampling the collected MRI data, and (iii) the calculation of the Intensity-Curvature Measurement Approaches.

The working hypothesis of the works herein reported is: 'to see as to if the complementary and/or additional information extracted from the collected MRI is useful in MRI diagnostic settings'. The results reported in this paper signify that it is possible, through the use of the Intensity-Curvature Measurement Approaches, to extract from the MRI images, information which is complementary and/or additional, and also useful to the diagnosis of the tumor detected with MRI.

Methodology

Subjects

This work presents case studies on eleven patients suffering from tumors in the human brain. The subjects were: (i) a 40 years old female (metastases), (ii) a 77 years old male (glioblastoma multiforme), (iii) a 33 years old female (intraventricular brain tumor), (iv) a 64 years old male (oligodendroglioma), (v) a 72 years old male (brain metastases), (vi) a 55 years old male (brain metastases from pulmonary cancer), (vii) a 41 years old female (anaplastic oligodendroglioma), (viii) a 38 years old female (meningioma), (ix) a 37 years old female (cystic glioblastoma), (x) a 44 years old female (glioblastoma), (xi) a 42 years old male (tumor with intraventricular extension). *Compliance with the declaration of Helsinki and the obtainment of the informed consent is assured because of the fact that the subject had the MRI collected for clinical inspection purposes. The informed consent was administered after proper explanation of the purpose of the MRI scanning.*

MRI modalities

Generally, the choice of the technical characteristics of the MRI modalities such as: T1-weighted MRI with or without contrast agent, T2-weighted MRI, FLAIR pulse sequence; has been made with the specific intention to image the brain tumors at best. In reference to the metastases this manuscript reports: (i) a coronal T2-weighted MRI (see Fig. 4a), (ii) a FLAIR pulse sequence MRI in the transverse plane (see Fig. 5a), (iii) a T2-weighted MRI in the transverse plane (see Fig. 6a), (iv) a coronal contrast enhanced T1-weighted MRI (see Fig. 7a), (v) a contrast enhanced T1-weighted MRI in the transverse plane (see Fig. 17c), (vi) a T2-weighted MRI in the transverse plane (see Fig. 18a). In reference to the glioblastoma this manuscript reports: (i) a coronal T2-weighted MRI (see Fig. 8a), (ii) a T2-weighted MRI in the transverse plane (see Fig. 9a), (iii) a contrast enhanced T1-weighted MRI in the transverse plane (see Fig. 10a), (iii) a coronal plane contrast enhanced T1-weighted MRI (see Fig. 11a), (iv) a contrast enhanced T1-weighted MRI in the sagittal plane (see

Fig. 17g), (v) a FLAIR MRI in the transverse plane (see Fig. 19a). In reference to the intraventricular brain tumor this manuscript reports: (i) a sagittal T1-weighted MRI (see Fig. 12a), (ii) a FLAIR pulse sequence image in the transverse plane (see Fig. 13a), (iii) a contrast enhanced T1-weighted MRI in the transverse plane (see Fig. 14a), (iv) a contrast enhanced T1-weighted MRI in the transverse plane (see Fig. 15a), (v) a contrast enhanced T1-weighted MRI in the transverse plane (see Fig. 17i). Fig. 16a shows a T1-weighted MRI image in the sagittal plane. In reference to the other pathologies studied, this manuscript reports: (i) two coronal contrast enhanced T1-weighted MRI of the oligodendroglioma (see Fig. 17a and e respectively), and (ii) a contrast enhanced T1-weighted MRI of the meningioma (see Fig. 18c).

The Intensity-Curvature Measurement Approaches

The Intensity-Curvature Measurement Approaches are: (i) the classic-curvature [21], (ii) the signal resilient to interpolation [22], (iii) the intensity-curvature measure [21] and (iv) the intensity-curvature functional [21]. Three subjects were studied in order to assess the potential of the Intensity-Curvature Measurement Approaches and to elucidate the main findings made through the study (see Figs. 4–16). Thus, in Figs. 4–15, each of the MRI is displayed together with the four post-processed images in the quest for additional information. Fig. 16 elucidates the *visually perceptible* third dimension of the classic-curvature and the intensity-curvature functional. Moreover, eight additional subjects were studied in order to seek for confirmation of the main findings (see Figs. 17–19). It will become clear in the results section that both the signal resilient to interpolation (in all of the tumor cases) and the classic-curvature (for the intra-ventricular tumor case) are those images which are capable of adding the most to the diagnosis made with the collected MRI.

Table 1 summarizes the following information relevant to the three subjects studied in order to assess the potential of the Intensity-Curvature Measurement Approaches. The classic-curvature (CC) has been obtained when fitting and re-sampling the MRI data with the bivariate cubic polynomial (re-sampling coordinate $(x, y) = (0.5 \text{ mm}, 0.5 \text{ mm})$ in the case of the metastates and also in the case of the glioblastoma multiforme). In the case of the intraventricular brain tumor, the bivariate cubic polynomial had the re-sampling coordinate equal to $(x, y) = (0.25 \text{ mm}, 0.25 \text{ mm})$, and the bivariate cubic Lagrange polynomial had the re-sampling coordinate equal to $(x, y) = (0.1 \text{ mm}, 0.1 \text{ mm})$.

The signal resilient to interpolation (SRI) has been obtained when fitting the MRI data with the bivariate cubic Lagrange polynomial when re-sampling with $(x, y) = (0.1 \text{ mm}, 0.1 \text{ mm})$ in all of the three cases reported in Table 1: (i) metastases, (ii) glioblastoma multiforme and (iii) intraventricular brain tumor. Also, for the cases of the metastases and the glioblastoma multiforme, the intensity-curvature measure (ICM) has been obtained when fitting the monovariate sinc function to the MRI data and re-sampling with $x = 0.5 \text{ mm}$. Whereas, for the case of the intraventricular brain tumor, the intensity-curvature measure had the re-sampling coordinate equal to $x = 0.25 \text{ mm}$.

The bivariate linear function has been used to calculate the intensity-curvature functional (ICF) with the re-sampling
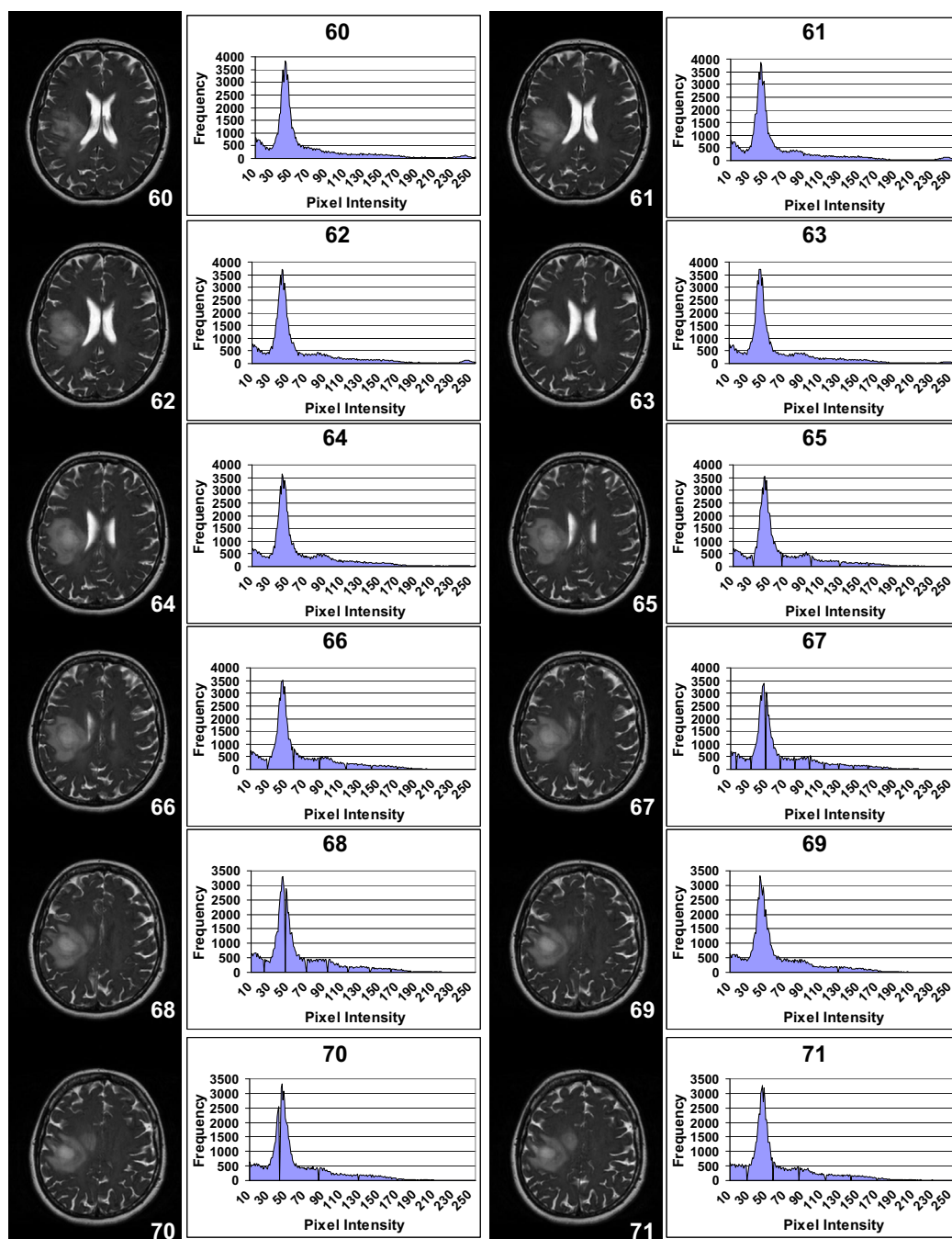
Fig. 1 A variant of the plane T2-weighted MRI (T2-TSE-3D-TRA-P2) showing the metastases (slices 60 through 71). The tumor shows a pattern of propagation that appears to have features of circularity and this is visible across the slices. The recording parameters of the pulse sequence are detailed as follows. Echo time (TE) = 109 ms, repetition time (TR) = 750 ms, pixel matrix size = 512 · 512 and pixel size = 0.49 mm · 0.49 mm. The histograms show the frequency of occurrence of each pixel intensity value. To calculate the histograms, the pixel intensity values were scaled in the range $[0, 255]$.

coordinate equal to $x = 0.25$ mm in the case of the intraventricular tumor and the re-sampling coordinate equal to $x = 0.5$ mm in the cases of metastases, and glioblastoma multiforme.

Although re-sampling is possible at an immense number of intra-pixel re-sampling locations, the values herein reported where chosen on the basis of previous experience, and with the aim to obtain high quality post-processed images.

Hereto follow are reported the Pathologies/Formulae/ Measures relevant to the additional eight subjects studied in order to seek for confirmation of the main findings. The Intensity-Curvature Measurement Approaches are: (i) the classic-curvature (CC) calculated with the bivariate cubic polynomial so as to study the brain metastases (see Fig. 17d), (ii) the intensity-curvature functional (ICF) calculated with the bivariate linear function so as to study the
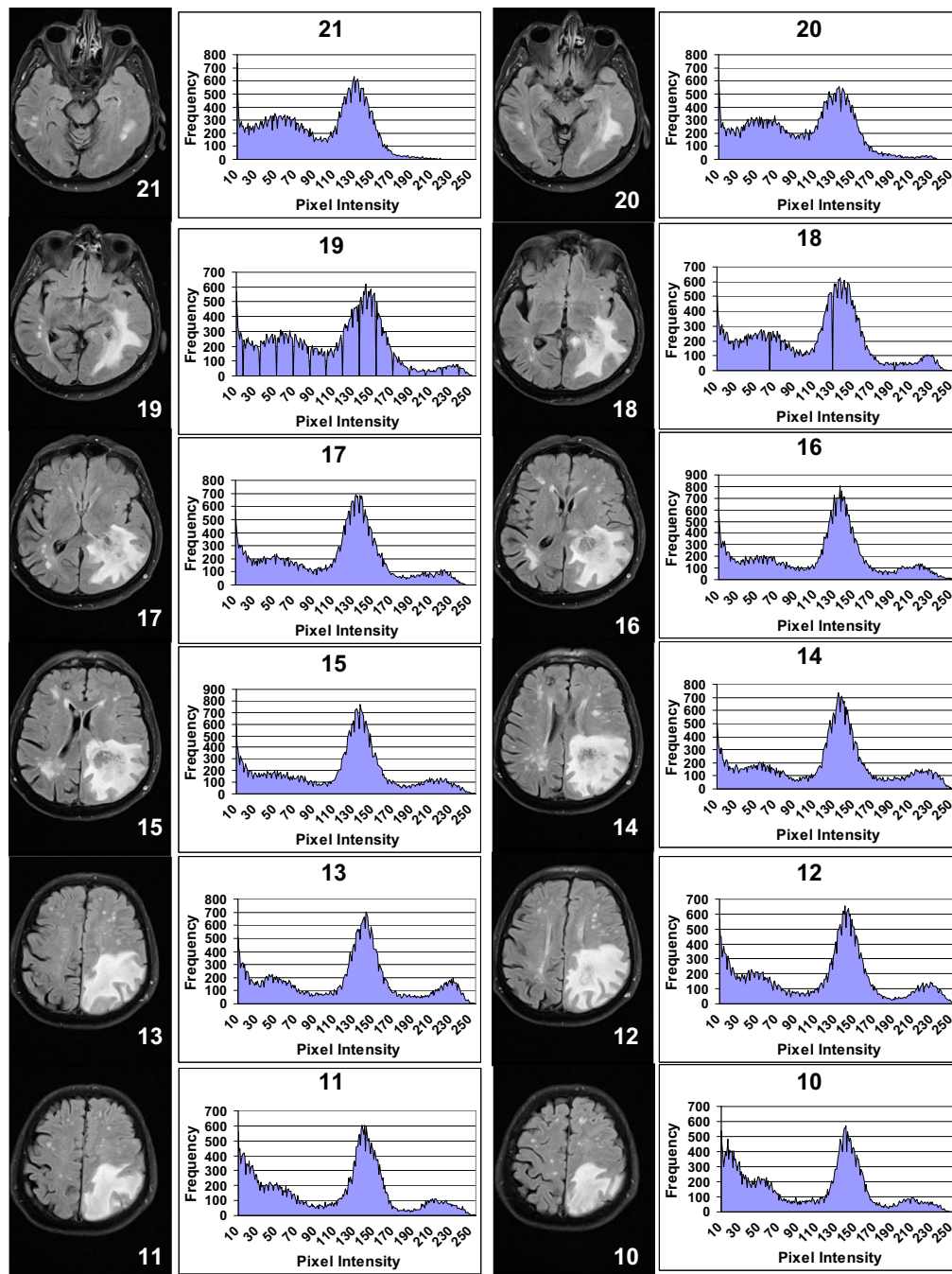
Fig. 2 FLAIR pulse sequence MRI in the transverse plane showing the evolution and the propagation of the glioblastoma multiforme in the human brain (slices 21 through 10). The pathology shows a scattered pattern of propagation across slices, which is different from the one observed in Fig. 1 where the metastases is shown. The recording parameters of the pulse sequence are detailed as follows. Echo time (TE) = 84 ms, repetition time (TR) = 9000 ms, pixel matrix size = 260 · 320 and pixel size = 0.73 mm · 0.73 mm. The histograms show the frequency of occurrence of each pixel intensity value. To calculate the histograms, the pixel intensity values were scaled in the range [0, 255].

glioblastoma (see Fig. 17h), the brain metastases from pulmonary cancer (see Fig. 18b), the meningioma (see Fig. 18d), and the cystic glioblastoma (see Fig. 19b), and (iii) the signal resilient to interpolation (SRI) calculated with the bivariate cubic Lagrange polynomial so as to study the oligodendroglioma (see Fig. 17b), the anaplastic oligoden-

droglioma (see Fig. 17f), and the tumor with intraventricular extension (see Fig 17j). The re-sampling coordinate applied to the pathologies when fitting the formulae to the collected MRI was 0.1 mm (bivariate cubic Lagrange polynomial), 0.5 mm (bivariate cubic polynomial), 0.5 mm (bivariate linear function).
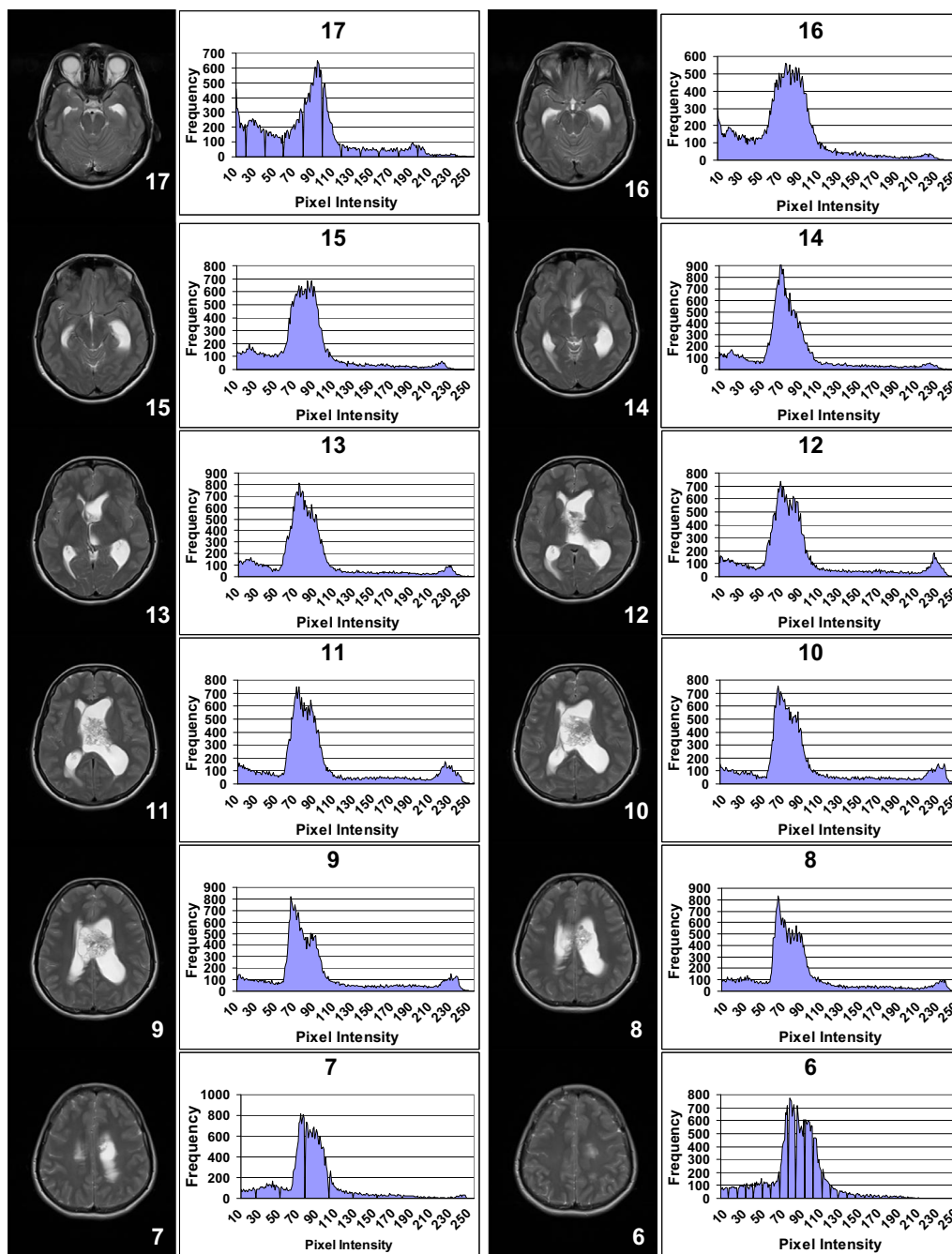
Fig. 3   Plane T2-weighted MRI showing the pathology of the human brain called intraventricular brain tumor (slices 17 through 6). As visible across the slices, the pattern of propagation of the pathology has a well defined feature which is that of attacking the ventricles of the human brain. The recording parameters of the pulse sequence are detailed as follows. Echo time (TE) = 96 ms, repetition time (TR) = 4720 ms, pixel matrix size = 252 · 320 and pixel size = 0.78 mm · 0.78 mm. The histograms show the frequency of occurrence of each pixel intensity value. To calculate the histograms, the pixel intensity values were scaled in the range [0, 255].

The mathematical formulation

Hereto follow is reported the mathematical formulation employed in the works presented in the manuscript. The bivariate cubic polynomial is found in [22] and is here reported:

$$f(x,y) = f(0,0) + [f(1,0) - f(0,0)](ax^2 + y)$$
$$+ [f(0,1) - f(0,0)](by^2 - x) + [f(1,1)$$
$$+ f(0,0) - f(0,1) - f(1,0)](ax^2y + by^2x) \quad (1)$$

where $f(1,0), f(1,0), f(1,1)$ are the values of the pixel intensities of the neighbors of $f(0,0)$, which is the pixel to re-sample. The classic-curvature $Y_c(x, y)$ of the bivariate cubic polynomial (1) is also found in [22]:

$$Y_c(x,y) = \left(\frac{\partial^2 f(x,y)}{\delta x^2}\right) + \left(\frac{\partial^2 f(x,y)}{\delta y^2}\right) + \left(\frac{\partial^2 f(x,y)}{\partial x \partial y}\right) + \left(\frac{\partial^2 f(x,y)}{\partial y \partial x}\right)$$
$$= \varphi_a(2a) + \varphi_{ab}(2ay) + \varphi_b(2b) + \varphi_{ab}(2bx)$$
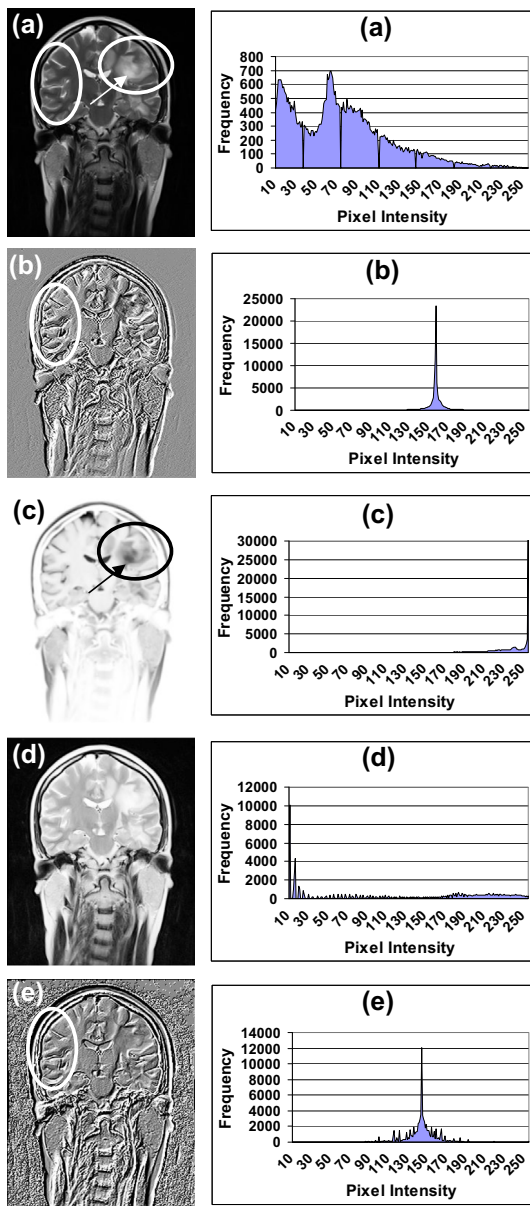$$+ 2\varphi_{ab}(2ax + 2by) \quad (2)$$

Fig. 4 In (a) is shown a coronal T2-weighted MRI. The recording parameters of the pulse sequence are detailed as follows. Echo time (TE) = 96 ms, repetition time (TR) = 5050 ms, pixel matrix size = 262 · 320 and pixel size = 0.78 mm · 0.78 mm. The ellipses in (a), (b) and (e) highlight normal brain structures and their reproduction with a third dimension perpendicular to the image plane. The ellipse and the arrow in (a) and (c) show that the signal resilient to interpolation image can be such that to confirm the anomaly and to display the anomaly with various gray levels and such fact can add additional information to the diagnosis, which is normally performed with the collected MRI shown in (a). The histograms located at the right of the brain images show the frequency of occurrence of each pixel intensity value. To calculate the histograms, the pixel intensity values were scaled in the range [0, 255]. The values of the Kolmogorov–Smirnov test D_n (result of the test) and D (critical value) were: 0.2085, 0.005 in the histogram in (b), and 0.113, 0.005 in the histogram in (e).
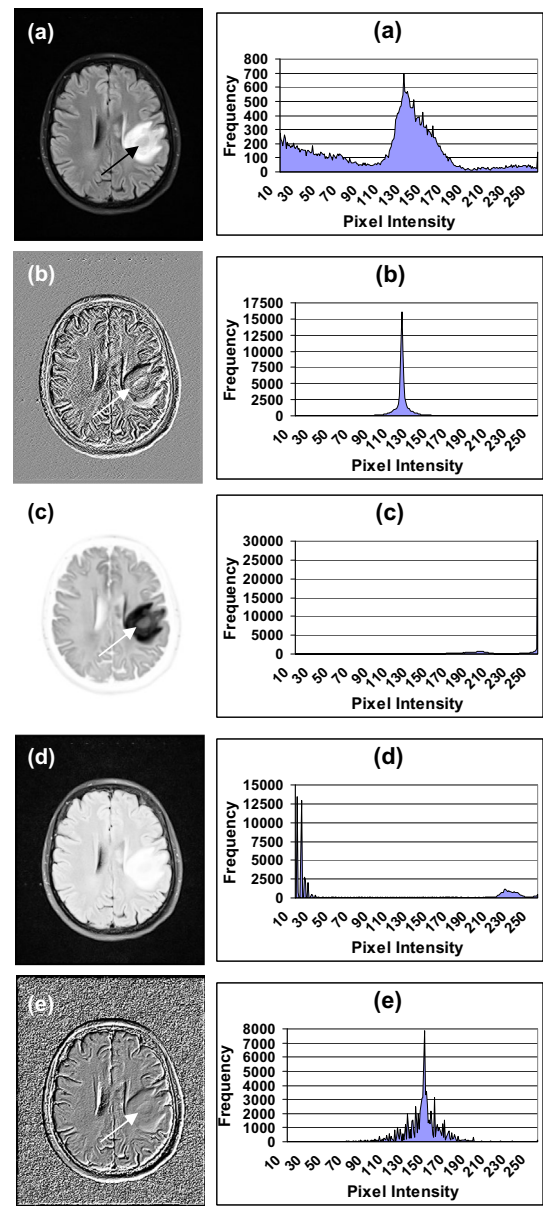
Fig. 5 In (a) is shown a FLAIR pulse sequence MRI in the transverse plane. The recording parameters of the pulse sequence are detailed as follows. Echo time (TE) = 84 ms, repetition time (TR) = 9000 ms, pixel matrix size = 260 · 320 and pixel size = 0.78 mm · 0.78 mm. The signal resilient to interpolation (c) acts as image enhancement tool when compared to the collected MRI shown in (a). The classic-curvature and the intensity-curvature functional images shown in (b) and in (e) respectively, extract the third dimension of the tumor mass indicated by the arrow. The intensity-curvature measure image focuses on the highlight of the spatial extent of the tumor mass. The histograms show the frequency of occurrence of each pixel intensity value. To calculate the histograms, the pixel intensity values were scaled in the range [0, 255]. The values of the Kolmogorov–Smirnov test D_n (result of the test) and D (critical value) were: 0.196, 0.005 in the histogram in (b), and 0.091, 0.005 in the histogram in (e).
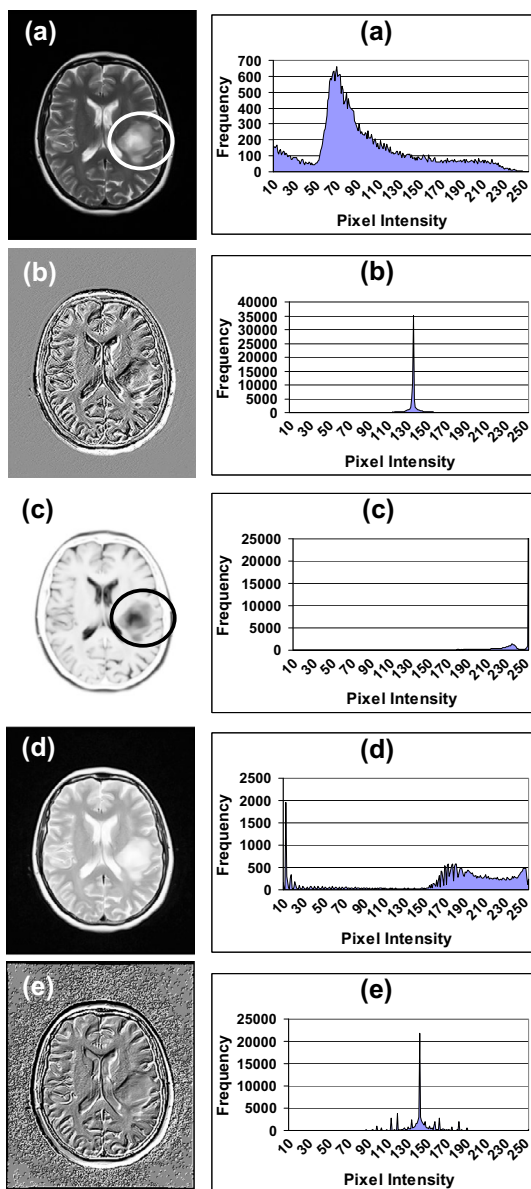
Fig. 6 In (a) is shown a T2-weighted MRI in the transverse plane. The recording parameters of the pulse sequence are detailed as follows. Echo time (TE) = 96 ms, repetition time (TR) = 4720 ms, pixel matrix size = 262 · 320 and pixel size = 0.78 mm · 0.78 mm. Another example of how the signal resilient to interpolation (see (c)) can be supportive to the diagnosis made through the collected MRI (shown in (a)), while presenting the tumor mass with a varied array of grayscale colors. The intensity-curvature measure image indicates the tumor external contour line (see (d)). The classic-curvature (CC) image and the intensity-curvature functional (ICF) image build the *visually perceptible* third dimension of the tumor mass (see CC in (b) and ICF in (e)). The histograms show the frequency of occurrence of each pixel intensity value. To calculate the histograms, the pixel intensity values were scaled in the range [0, 255]. The values of the Kolmogorov–Smirnov test D_n (result of the test) and D (critical value) were: 0.2853, 0.005 in the histogram in (b), and 0.17, 0.005 in the histogram in (e).
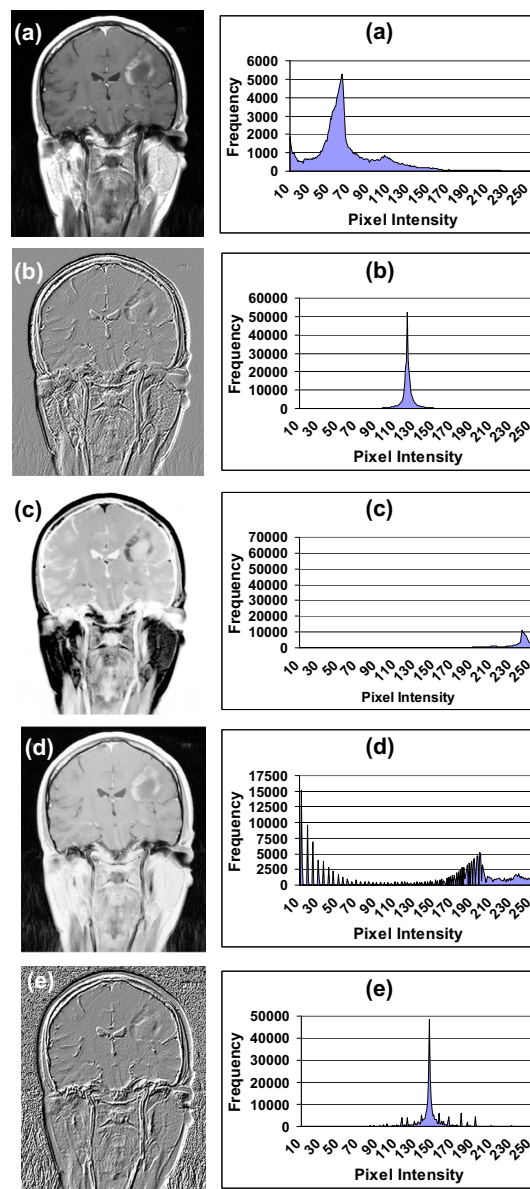
Fig. 7 In (a) is shown a coronal contrast enhanced T1-weighted MRI. The recording parameters of the pulse sequence are detailed as follows. Echo time (TE) = 9 ms, repetition time (TR) = 550 ms, pixel matrix size = 512 · 512 and pixel size = 0.45 mm · 0.45 mm. In (c) and in (d) the signal resilient to interpolation and the intensity-curvature measure images show complementary information to the collected MRI shown in (a), whereas in (b) and in (d) the classic-curvature and the intensity-curvature functional images provide the collected MRI with additional information pertinent to the third dimension. The histograms show the frequency of occurrence of each pixel intensity value. To calculate the histograms, the pixels intensity values were scaled in the range [0, 255]. The values of the Kolmogorov–Smirnov test D_n (result of the test) and D (critical value) were: 0.1785, 0.003 in the histogram in (b), and 0.2051, 0.003 in the histogram in (e).
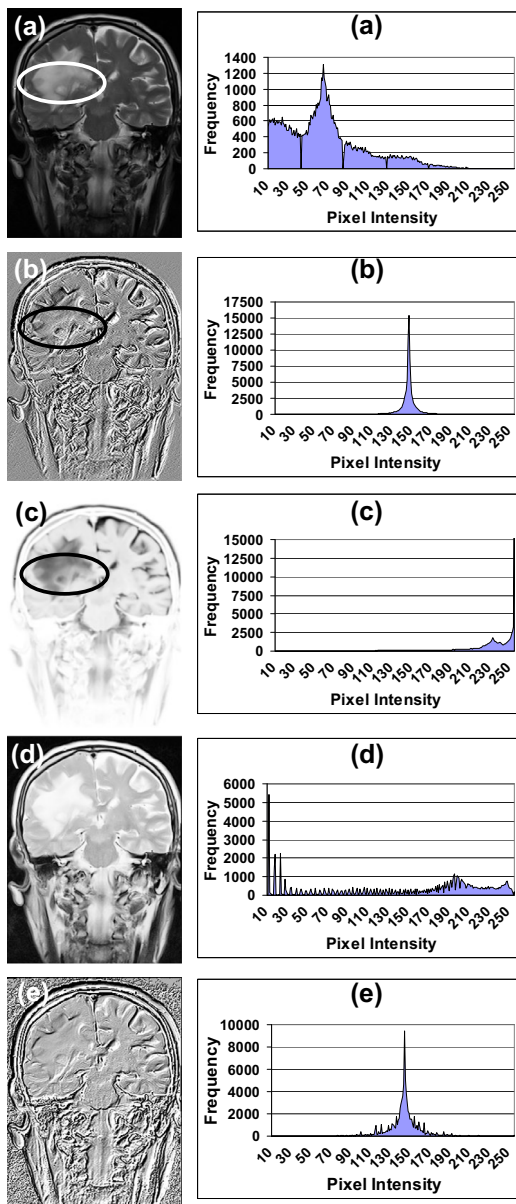
Fig. 8 In (a) is shown a coronal T2-weighted MRI. The recording parameters of the pulse sequence are detailed as follows. Echo time (TE) = 96 ms, repetition time (TR) = 5050 ms, pixel matrix size = 262 · 320 and pixel size = 0.72 mm · 0.72. In (b) and in (e) are visible tumor structures and in (c) the tumor structures are visible with a different grayscale (see inside the ellipses). In (d) and in (e), the extension of the tumor can be seen in white (see (d)) and with a higher elevation (see (e)), and in both of the images it can be distinguished the external contour line as well as the spatial extent internal to the contour line. The histograms show the frequency of occurrence of each pixel intensity value. To calculate the histograms, the pixel intensity values were scaled in the range [0, 255]. The values of the Kolmogorov–Smirnov test D_n (result of the test) and D (critical value) were: 0.1781, 0.005 in the histogram in (b), and 0.1212, 0.005 in the histogram in (e).

Fig. 9 In (a) is shown a T2-weighted MRI in the transverse plane. The recording parameters of the pulse sequence are detailed as follows. Echo time (TE) = 109 ms, repetition time (TR) = 750 ms, pixel matrix size = 512 · 512 and pixel size = 0.45 mm · 0.45 mm. In the case shown in (c) the tumor structures are more clearly demarcated than the collected MRI seen in (a) (see inside the ellipses), whereas (b), (d) and (e) confirm the observations that can be made through (a) and (c). The histograms show the frequency of occurrence of each pixel intensity value. To calculate the histograms, the pixel intensity values were scaled in the range [0, 255]. The values of the Kolmogorov–Smirnov test D_n (result of the test) and D (critical value) were: 0.2088, 0.003 in the histogram in (b), and 0.1837, 0.003 in the histogram in (e).
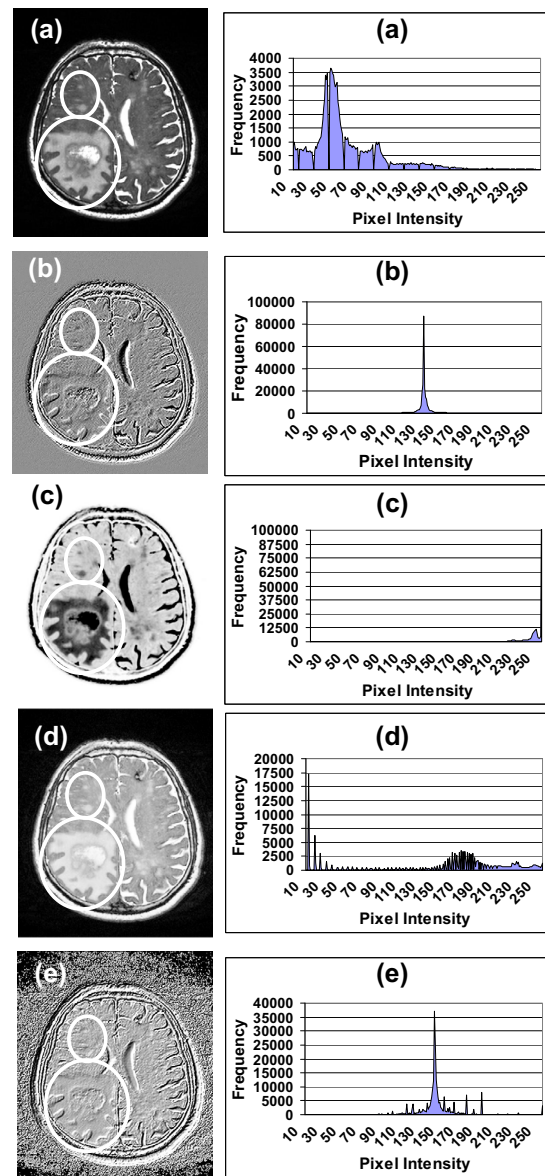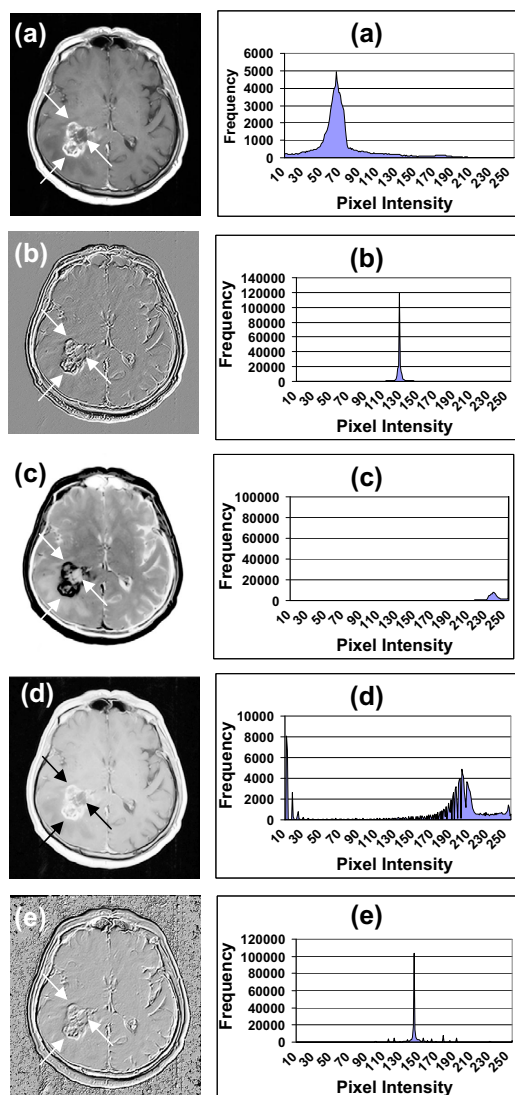
Fig. 10 In (a) is shown a contrast enhanced T1-weighted MRI in the transverse plane. The recording parameters of the pulse sequence are detailed as follows. Echo time (TE) = 8.7 ms, repetition time (TR) = 680 ms, pixel matrix size = 512 · 512 and pixel size = 0.48 mm · 0.48 mm. The most interesting aspects illustrated in the images are: (i) the tumor contour line observable in (b) and in (e) and the subdivision of the tumor mass into sectors of different gray level scale observable in (c) and in (d). The arrows point to the tumor sectors with each figure highlighting the most prominent aspect of the information provided to the collected MRI. The histograms show the frequency of occurrence of each pixel intensity value. To calculate the histograms, the pixel intensity values were scaled in the range [0, 255]. The values of the Kolmogorov–Smirnov test D_n (result of the test) and D (critical value) were: 0.2561, 0.003 in the histogram in (b), and 0.327, 0.003 in the histogram in (e).

Fig. 11 In (a) is shown a coronal plane contrast enhanced T1-weighted MRI. The recording parameters of the pulse sequence are detailed as follows. Echo time (TE) = 8.7 ms, repetition time (TR) = 680 ms, pixel matrix size = 512 · 512 and pixel size = 0.48 mm · 0.48 mm. Similarly to what seen in Fig. 7 the emphasis of the images here presented is in: (i) the *visually perceptible* third dimension and the tumor contour line visible in (b) and in (e), and (ii) the division of the tumor in regions surrounded by the white color in (a) and (d) and by the dark color in (c). The histograms show the frequency of occurrence of each pixel intensity value. To calculate the histograms, the pixels intensity values were scaled in the range [0, 255]. The values of the Kolmogorov–Smirnov test D_n (result of the test) and D (critical value) were: 0.2301, 0.003 in the histogram in (b), and 0.2772, 0.003 in the histogram in (e).
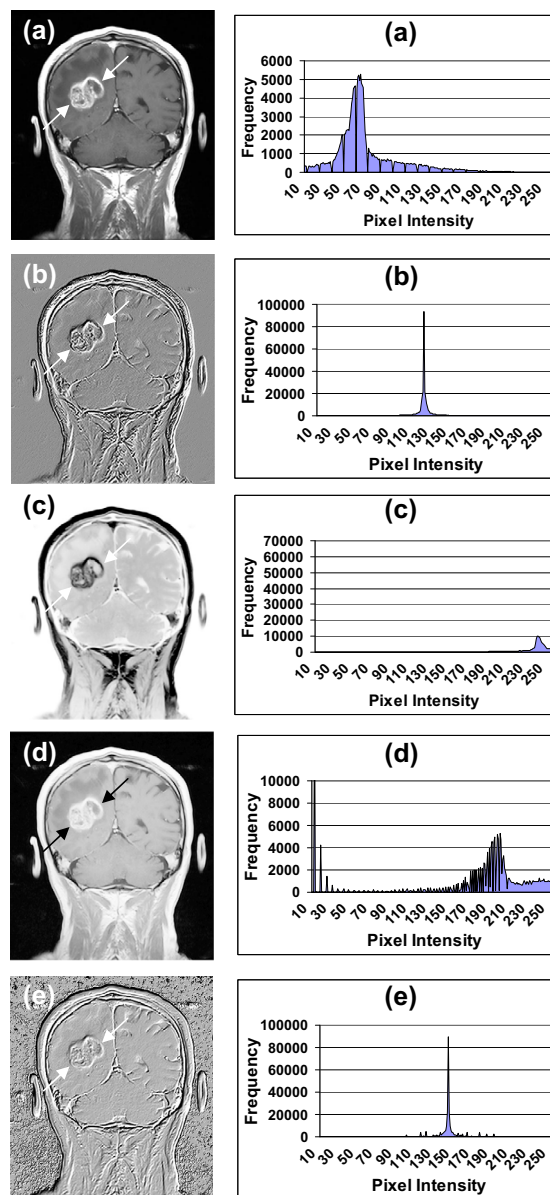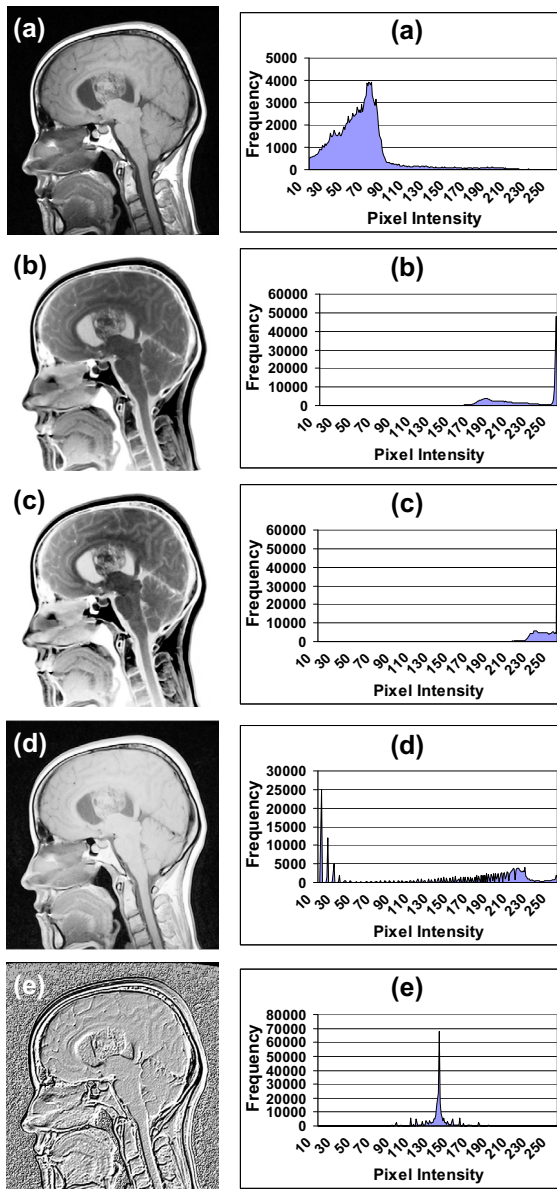
Fig. 12 In (a) is shown a sagittal T1-weighted MRI. The recording parameters of the pulse sequence are detailed as follows. Echo time (TE) = 8.7 ms, repetition time (TR) = 550 ms, pixel matrix size = 512 · 512 and pixel size = 0.45 mm · 0.45 mm. The key to making a contribution to the diagnosis in this specific case is in the fact that the enhanced gray level scale of the tumor mass as shown in (b) and in (c) may unveil details not available in the image in (a). This possibility is offered through the gray levels that image the tumor both in (b) and in (c). The image in (d) does not provide with additional details, whereas the image in (e) is related to the geography of the tumor. The histograms show the frequency of occurrence of each pixel intensity value. To calculate the histograms, the pixel intensity values were scaled in the range [0, 255]. The values of the Kolmogorov–Smirnov test D_n (result of the test) and D (critical value) were: 0.1897, 0.003 in the histogram in (e). The histogram in (b) clearly does not suggest a Gaussian distribution.

Fig. 13 In (a) is shown a FLAIR pulse sequence image in the transverse plane. The recording parameters of the pulse sequence are detailed as follows. Echo time (TE) = 84 ms, repetition time (TR) = 9000 ms, pixel matrix size = 260 · 320 and pixel size = 0.78 mm · 0.78 mm. The tumor mass in (b) and in (c) is imaged with three predominant colors: white, black and gray offering a view which is complementary but not additional to the image of the MRI shown in (a). Similarly, through the contribution of both of the intensity-curvature measure image (d) and the intensity-curvature functional image (e), the information content is complementary to (a). The histograms show the frequency of occurrence of each pixel intensity value. To calculate the histograms, the pixels intensity values were scaled in the range [0, 255]. The values of the Kolmogorov–Smirnov test D_n (result of the test) and D (critical value) were: 0.1054, 0.005 in the histogram in (e). The histogram in (b) clearly does not suggest a Gaussian distribution.

Fig. 14 In (a) is shown a contrast enhanced T1-weighted MRI in the transverse plane. The recording parameters of the pulse sequence are detailed as follows. Echo time (TE) = 13 ms, repetition time (TR) = 477 ms, pixel matrix size = 256 · 320 and pixel size = 0.72 mm · 0.72 mm. Particularly interesting is the comparison of the images in (a), in (b) and in (c) which are complementary to each other (for instance, see the structure pointed by the white arrows), whereas the images in (a), in (d) and in (e) emphasize the loss of healthy tissue inside the ventricles because of the tumor mass (see inside the ellipse). The histograms show the frequency of occurrence of each pixel intensity value. To calculate the histograms, the pixel intensity values were scaled in the range [0, 255]. The values of the Kolmogorov–Smirnov test D_n (result of the test) and D (critical value) were: 0.1583, 0.005 in the histogram in (e). The histogram in (b) clearly does not suggest a Gaussian distribution.
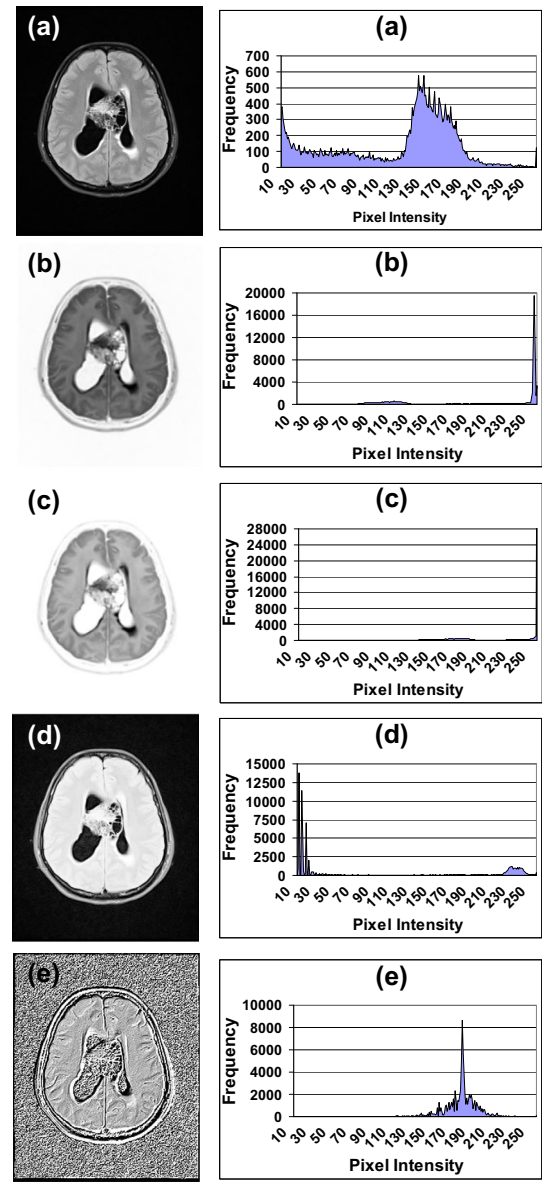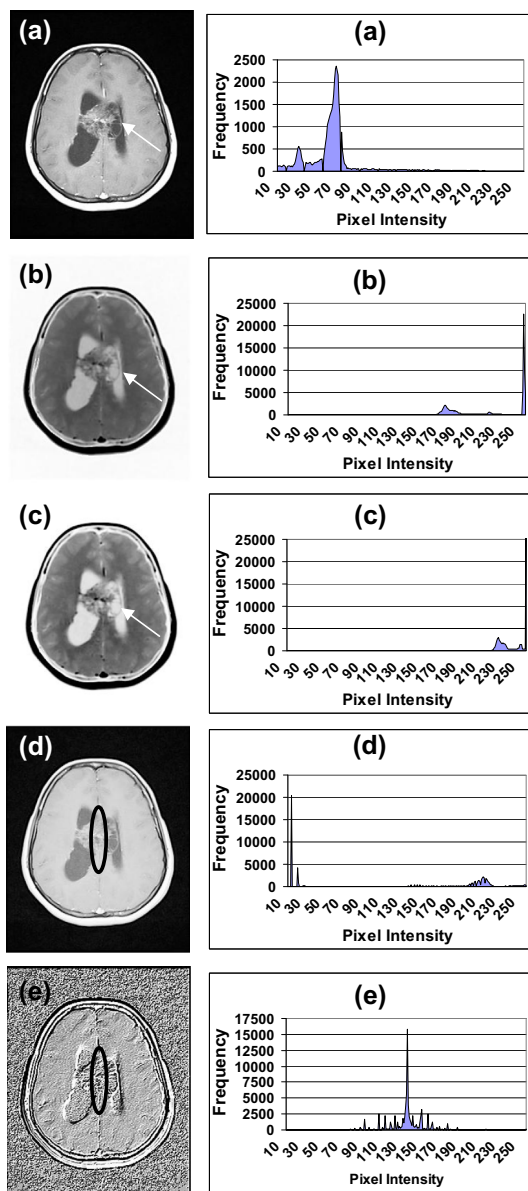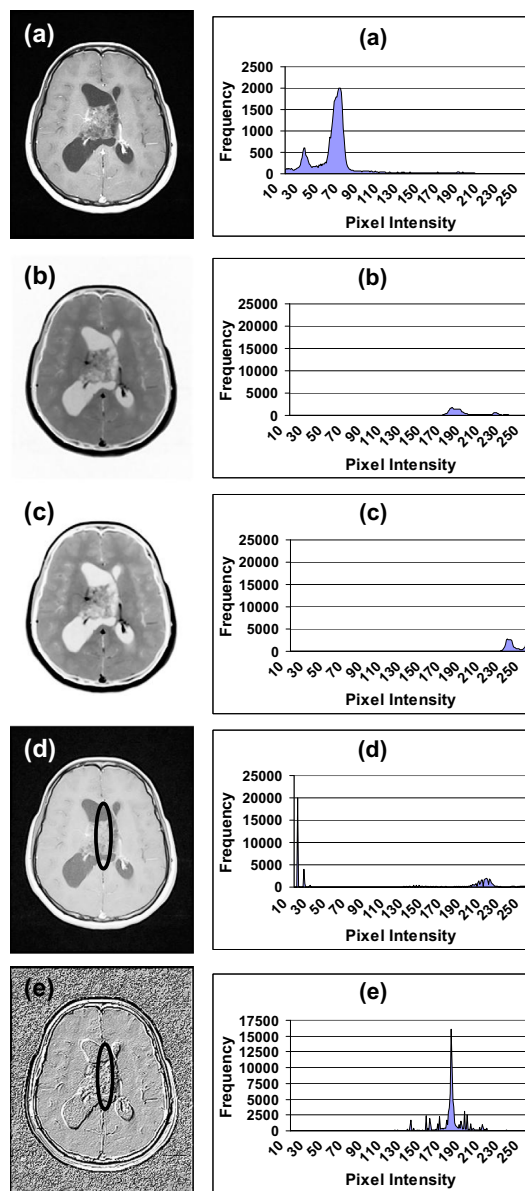
Fig. 15 In (a) is shown a contrast enhanced T1-weighted MRI in the transverse plane. The recording parameters of the pulse sequence are detailed as follows. Echo time (TE) = 13 ms, repetition time (TR) = 477 ms, pixel matrix size = 256 · 320 and pixel size = 0.72 mm · 0.72 mm. Complementary information to the one observable in (a) is provided in (b) and in (c). And (d), (e) confirm that the healthy intra-ventricular tissue is affected because of the tumor (see inside the ellipse). The histograms show the frequency of occurrence of each pixel intensity value. To calculate the histograms, the pixel intensity values were scaled in the range [0, 255]. The values of the Kolmogorov–Smirnov test D_n (result of the test) and D (critical value) were: 0.2847, 0.005 in the histogram in (e). The histogram in (b) clearly does not suggest a Gaussian distribution.
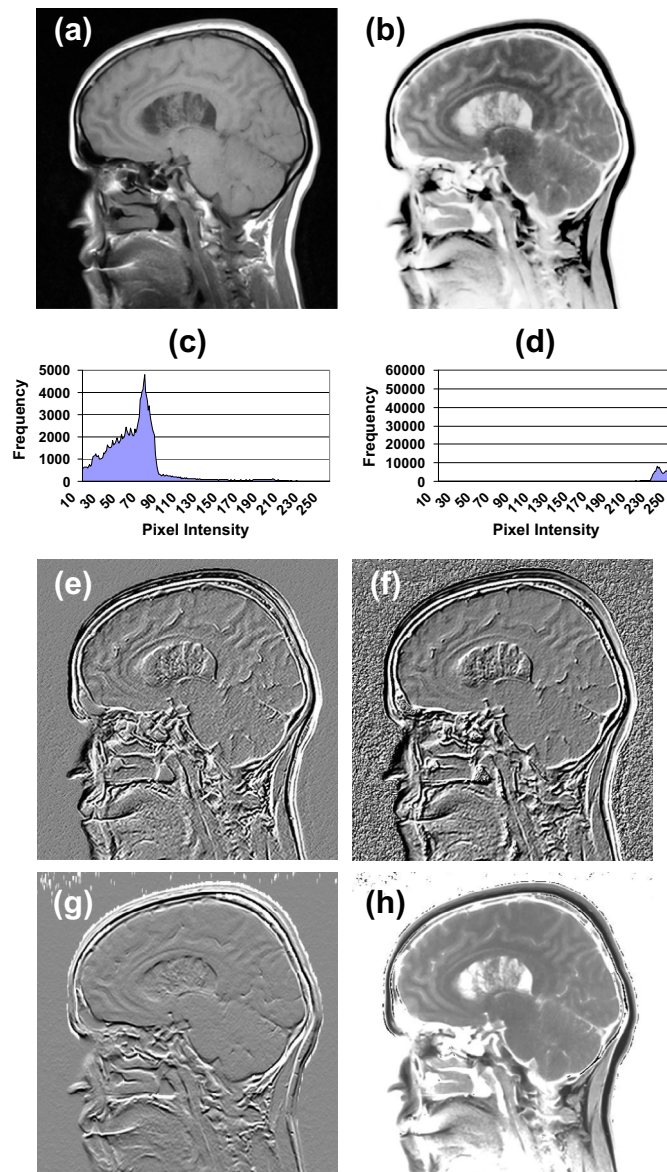
Fig. 16 The original T1-weighted MRI is shown in (a) and in (b) is shown the SRI. The recording parameters were: Echo time (TE) = 8.7 ms, repetition time (TR) = 550 ms, pixel matrix size = 512 · 512 and pixel size = 0.45 mm · 0.45 mm. The SRI acts a post-processing tool capable to stretch the grayscale level of the collected MRI seen in (a), thus making possible to see in finer details the anatomy of both the brain and the intra-ventricular tumor structures. In other words, the SRI acts as an internal light bulb illuminating the MRI. The histograms seen in (c) and in (d) are relevant to the images shown in (a) and in (b) respectively. To calculate the histograms, the pixel intensity values were scaled in the range [0, 255]. In (e) is shown the classic-curvature calculated with the cubic bivariate polynomial and in (f) is shown the intensity-curvature functional calculated with the bivariate linear function. In (g) is shown the high pass filter mask calculated from the collected MRI in (a) and in (h) is shown the collected MRI filtered with the filter mask seen in (g).

With:

$$\varphi_a = [f(1,0) - f(0,0)] \quad (3)$$

$$\varphi_b = [f(0,1) - f(0,0)] \quad (4)$$

$$\varphi_{ab} = [f(1,1) + f(0,0) - f(0,1) - f(1,0)] \quad (5)$$

where $f(0,1), f(1,0), f(1,1)$ are values of pixels in the neighborhood of $f(0,0)$, which is the pixel to re-sample. The implicit form of the bivariate cubic Lagrange polynomial $g(\mathbf{x}) = g(x_1, x_2)$ is defined as:

$$g(\mathbf{x}) = f(\mathbf{0}) + \alpha_2 \cdot a \sum_{i=0}^{3} h_i \left(\sum_{k=1}^{n} x_k \right)^i + \alpha_3 \cdot a \sum_{i=0}^{2} m_i \left(\sum_{k=1}^{n} x_k \right)^i \quad (6)$$

The constant $f(\mathbf{0})$ is the pixel to re-sample, 'a' is the parameter of the cubic Lagrange polynomial, 'h_i' and 'm_i' are the coefficients of the polynomial, 'n' defines the dimensionality of the polynomial, 'i' is the exponent of each of the sums of the independent variables and α_2, α_3 are sums of pixel intensities in the proximity of the pixel to re-sample. Eq. (6) is found in [2]. The explicit form of the bivariate cubic Lagrange polynomial used in this research is defined as:
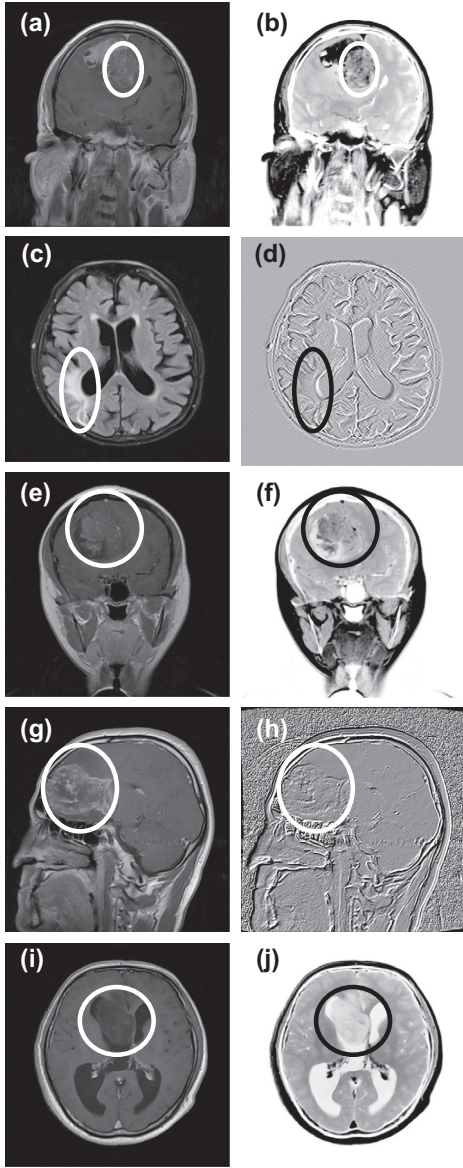
Fig. 17 Five different subjects all diagnosed with tumor in the brain. Contrast enhanced T1-weighted MRI images are shown in (a) (oligodendroglioma), in (c) (brain metastases), in (e) (anaplastic oligodendroglioma), in (g) (glioblastoma) and in (i) (tumor with intraventricular extension). The signal resilient to interpolation is shown in (b), (f) and (j) and it was calculated when using the bivariate cubic Lagrange polynomial. The images in (d) and (h) are classic-curvature and intensity-curvature functional respectively and were obtained using the bivariate cubic polynomial and the bivariate linear function. The recording parameters of the pulse sequences are detailed as follows. (a) Echo time (TE) = 8.7 ms, repetition time (TR) = 583 ms, pixel matrix size = 512 · 512 and pixel size = 0.45 mm · 0.45 mm. (c) Echo time (TE) = 13 ms, repetition time (TR) = 477 ms, pixel matrix size = 256 · 320 and pixel size = 0.72 mm · 0.72 mm. (e) Echo time (TE) = 9 ms, repetition time (TR) = 550 ms, pixel matrix size = 512 · 512 and pixel size = 0.45 mm · 0.45 mm. (g) Echo time (TE) = 8.7 ms, repetition time (TR) = 550 ms, pixel matrix size = 512 · 512 and pixel size = 0.45 mm · 0.45 mm. (i) Echo time (TE) = 8.7 ms, repetition time (TR) = 550 ms, pixel matrix size = 512 · 512 and pixel size = 0.45 mm · 0.45 mm.
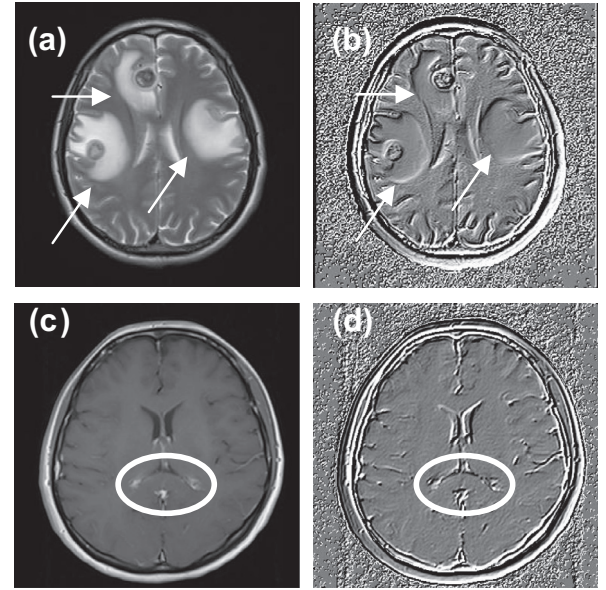
Fig. 18 Two subjects diagnosed with tumor in the brain. The diagnoses were: brain metastases from pulmonary cancer (a), and meningioma (c). In (a) is shown a T2-weighted MRI with the following recording parameters. Echo time (TE) = 96 ms, repetition time (TR) = 4720 ms, pixel matrix size = 262 · 320 and pixel size = 0.78 mm · 0.78 mm. In (c) is shown a contrast enhanced T1-weighted MRI with the following recording parameters. Echo time (TE) = 8.7 ms, repetition time (TR) = 550 ms, pixel matrix size = 512 · 512 and pixel size = 0.49 mm · 0.49 mm. In (b) and in (d) are shown the intensity-curvature functional images of (a) and (c) respectively and both of them were calculated using the bivariate linear function.

$$g(x,y) = f(0,0) + \alpha_2 \cdot a\left[(x+y)^3 + \frac{1}{2}(x+y)^2 + \frac{1}{4}(x+y) + 1\right]$$
$$+ \alpha_3 \cdot a\left[(x+y)^2 + 2(x+y) + 1\right] \tag{7}$$

With:

$$\alpha_2 = [f(1/2,1/2) + f(-1/2,-1/2) + f(2/3,2/3)$$
$$+ f(-2/3,-2/3) + f(-1,-1) + f(1,1)$$
$$+ f(3/2,3/2) + f(-3/2,-3/2)] \tag{8}$$
$$\alpha_3 = [f(1/2,1/2) + f(-1/2,-1/2) + f(-1,-1) + f(1,1)] \tag{9}$$

And $f(1/2,1/2)$, $f(-1/2,-1/2)$, $f(2/3,2/3)$, $f(-2/3,-2/3)$, $f(-1,-1)$, $f(1,1)$, $f(3/2,3/2)$, $f(-3/2,-3/2)$ are the values of the pixel intensities of the neighbors of $f(0,0)$, which is the pixel to re-sample. Eqs. (7)–(9) are found in [22]. The classic-curvature $CC(x, y)$ of the bivariate cubic Lagrange polynomial (7) is found in [22] and is here reported:

$$CC(x,y) = \left(\frac{\partial^2 g(x,y)}{\delta x^2}\right) + \left(\frac{\partial^2 g(x,y)}{\delta y^2}\right) + \left(\frac{\partial^2 g(x,y)}{\partial x \partial y}\right) + \left(\frac{\partial^2 g(x,y)}{\partial y \partial x}\right)$$
$$= 4 \cdot \{\alpha_2 \cdot a[6(x+y)+1] + 2\alpha_3 \cdot a\} \tag{10}$$

The signal resilient to interpolation $f(0,0)$ of the bivariate cubic Lagrange polynomial is found in [22] and it is here reported:

$$f(0,0) = \frac{\Lambda_{\mathrm{LGR}}}{\Theta_{\mathrm{LGR}}} \qquad (11)$$

where

$$\Theta_{\mathrm{LGR}} = [\alpha_2 \ a + 2 \ \alpha_3 \ a] \ xy$$
$$- \left[\alpha_2 \ a \ \left[6 \left(\frac{yx^2}{2} + \frac{xy^2}{2} \right) + xy \right] + 2 \ \alpha_3 \ a \ xy \right] \qquad (12)$$

$$\Lambda_{\mathrm{LGR}} = 6\varphi_4(\alpha_2 \ a)^2 + \varphi_3[4(\alpha_2 \ a)^2 + 8\alpha_3 \ \alpha_2 \ a^2] + \varphi_2 \ [\ 2(\alpha_2 \ a)^2 +$$
$$+ \ 14\alpha_3 \ \alpha_2 \ a^2 + 2(\alpha_3 \ a)^2] + \varphi_1 \ [\ \tfrac{25}{4}(\alpha_2 \ a)^2 + \tfrac{17}{2} \ \alpha_3 \ \alpha_2 \ a^2$$
$$+ \ 4(\alpha_3 \ a)^2] + [(\alpha_2 \ a)^2 + 3\alpha_3\alpha_2 \ a^2 + 2(\alpha_3 \ a)^2] \ xy \qquad (13)$$

$$\varphi_1 = \left(\frac{1}{2} yx^2 + \frac{1}{2} xy^2 \right) \qquad (14)$$

$$\varphi_2 = \left(\frac{1}{3} yx^3 + \frac{1}{2} x^2 y^2 + \frac{1}{3} xy^3 \right) \qquad (15)$$

Fig. 19 A single subject's FLAIR MRI diagnosed with cystic glioblastoma is shown in (a). The MRI acquisition was performed with the following recording parameters. Echo time (TE) = 84 ms, repetition time (TR) = 9000 ms, pixel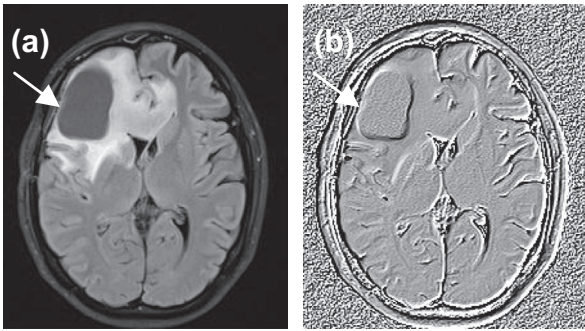 matrix size = 260 · 320 and pixel size = 0.78 mm · 0.78 mm. In (b) is shown the intensity-curvature functional of (a) calculated with the bivariate linear function.

$$\varphi_3 = \left(\frac{1}{4} yx^4 + \frac{1}{2} x^3 y^2 + \frac{1}{2} x^2 y^3 + \frac{1}{4} xy^4 \right) \qquad (16)$$

$$\varphi_4 = \left(\frac{1}{5} yx^5 + \frac{1}{2} x^4 y^2 + \frac{2}{3} x^3 y^3 + \frac{1}{2} x^2 y^4 + \frac{1}{5} xy^5 \right) \qquad (17)$$

where α_2 and α_3 are defined in Eqs. (8) and (9). The formulation of the monovariate Sinc function was selected from [23], and is found in [21] with the neighborhood being defined within $[-L, M]$; with $L + M = N$. For N odd number of neighboring nodes and with the sampling frequency $f_0 = (1/NT)$, the function assumes the following characterization:

$$h_O(x) = \sum_{n=-L}^{M-1} f(nT) \cdot \left(\frac{1}{N} \right) \cdot \left[1 + 2 \cdot \sum_{m=1}^{(N-1)/2} \cos(2\pi m f_0 x) \right] \qquad (18)$$

The intensity-curvature measure $\mathrm{ICM}(x)$ of $h_O(x)$ with $T = 1$ is found in [24] and is here reported where NEI is the size of the neighborhood (number of pixels to include in the calculation).

$$\mathrm{ICM}(x) = \frac{E_{\mathrm{IN}}(x_{\mathrm{SRE}} - x)}{E_{\mathrm{IN}}(x_{\mathrm{SRE}})} \qquad (19)$$

$$E_{\mathrm{IN}}(x_{\mathrm{SRE}}) = -\frac{\theta_2^2}{2} \cdot \left[\sum_{k=1}^{(N-1)/2} \theta_{4k} \cdot \sin\left(\frac{2\pi k}{\mathrm{NEI}} \right) \cdot x_{\mathrm{SRE}} \right]$$
$$- \theta_2^2 \cdot \sum_{k=1}^{(N-1)/2} \left[\left(\theta_{3k} \cdot \cos\left(\frac{2\pi k}{\mathrm{NEI}} \right) \cdot x_{\mathrm{SRE}} \right) \right.$$
$$\left. \cdot \left[\sum_{k=1}^{(N-1)/2} \left(\sin\left(\frac{2\pi k}{\mathrm{NEI}} \right) \cdot x_{\mathrm{SRE}} \right) \right] \right]$$
$$- \theta_2^2 \cdot \sum_{k=1}^{(N-1)/2} \left[\left(\theta_{3k} \cdot \sin\left(\frac{2\pi k}{\mathrm{NEI}} \right) \cdot x_{\mathrm{SRE}} \right) \right.$$
$$\left. \cdot \left[\sum_{k=1}^{(N-1)/2} \left(\cos\left(\frac{2\pi k}{\mathrm{NEI}} \right) \cdot x_{\mathrm{SRE}} \right) \right] \right] - \frac{\theta_2^2}{2} \cdot \left[\sum_{k=1}^{(N-1)/2} \theta_{3k} \right.$$
$$\left. \cdot \left[\sum_{k=1}^{(N-1)/2} \left(\sin\left(\frac{2\pi k}{\mathrm{NEI}} \right) \cdot x_{\mathrm{SRE}} \cdot \cos\left(\frac{2\pi k}{\mathrm{NEI}} \right) \cdot x_{\mathrm{SRE}} \right) \right]$$
$$\qquad (20)$$

Table 1 Pathologies/Formulae/Measures relevant to the three subjects studied to assess the potential of the Intensity-Curvature Measurement Approaches. The Intensity-Curvature Measurement Approaches are: the classic-curvature (CC), the intensity-curvature functional (ICF), the signal resilient to interpolation (SRI), and the intensity-curvature measure (ICM). The re-sampling coordinate applied to the pathologies when fitting the formulae to the collected MRI is reported in each entry of the table.

Pathologies/ Formulae/Measures	Bivariate cubic polynomial	Bivariate cubic Lagrange polynomial	Monovariate sinc function	Bivariate linear function
Metastases	CC, (x, y) = (0.5 mm, 0.5 mm)	SRI, (x, y) = (0.1 mm, 0.1 mm)	ICM, x = 0.5 mm	ICF, (x, y) = (0.5 mm, 0.5 mm)
Glioblastoma multiforme	CC, (x, y) = (0.5 mm, 0.5 mm)	SRI, (x, y) = (0.1 mm, 0.1 mm)	ICM, x = 0.5 mm	ICF, (x, y) = (0.5 mm, 0.5 mm)
Intraventricular brain tumor	CC, (x, y) = (0.25 mm, 0.25 mm)	SRI, (x, y) = (0.1 mm, 0.1 mm); CC, (x, y) = (0.1 mm, 0.1 mm)	ICM, x = 0.25 mm	ICF, (x, y) = (0.25 mm, 0.25 mm)

$$E_{\text{IN}}(x_{\text{SRE}} - x) = -\frac{\theta_2^2}{2} \cdot \left[\sum_{k=1}^{(N-1)/2} \theta_{4k} \cdot \sin\left(\frac{2\pi k}{\text{NEI}}\right) \cdot (x_{\text{SRE}} - x) \right]$$

$$- \theta_2^2 \cdot \sum_{k=1}^{(N-1)/2} \left[\left(\theta_{3k} \cdot \cos\left(\frac{2\pi k}{\text{NEI}}\right) \cdot (x_{\text{SRE}} - x) \right) \right.$$

$$\left. \cdot \left[\sum_{k=1}^{(N-1)/2} \left(\sin\left(\frac{2\pi k}{\text{NEI}}\right) \cdot (x_{\text{SRE}} - x) \right) \right] \right]$$

$$- \theta_2^2 \cdot \sum_{k=1}^{(N-1)/2} \left[\left(\theta_{3k} \cdot \sin\left(\frac{2\pi k}{\text{NEI}}\right) \cdot (x_{\text{SRE}} - x) \right) \right.$$

$$\left. \cdot \left[\sum_{k=1}^{(N-1)/2} \left(\cos\left(\frac{2\pi k}{\text{NEI}}\right) \cdot (x_{\text{SRE}} - x) \right) \right] \right]$$

$$- -\frac{\theta_2^2}{2} \cdot \left[\sum_{k=1}^{(N-1)/2} \theta_{3k} \right]$$

$$\cdot \left[\sum_{k=1}^{(N-1)/2} \left(\sin\left(\frac{2\pi k}{\text{NEI}}\right) \cdot \cos\left(\frac{2\pi k}{\text{NEI}}\right) \right.\right.$$

$$\left.\left. \cdot (x_{\text{SRE}} - x)^2 \right) + \left(\frac{2\pi k}{\text{NEI}}\right)(x_{\text{SRE}} - x) \right] \qquad (21)$$

$$\theta_{3k} = \left(\frac{2\pi k}{\text{NEI}}\right) \qquad (22)$$

$$\theta_{4k} = \left(\frac{2\pi k}{\text{NEI}}\right)^2 \qquad (23)$$

$$\theta_2 = \left[\sum_{k=-\text{NEI}/2}^{\text{NEI}/2} f(x_k) \cdot g(f(x_k)) \right] \cdot \left(\frac{2}{\text{NEI}}\right) \qquad (24)$$

The intensity-curvature measure [21] consists of the ratio between two terms (see Eq. (19)). The term at the numerator is the signal-image intensity-curvature content calculated at the coordinate obtained by the spatial difference between the sub-pixel efficacy region coordinate (x_{SRE}) [21] and the re-sampling coordinate (x). And the aforementioned term is called the relativity term (conveys the meaning of change). The term at the denominator is the signal-image intensity-curvature content calculated at the sub-pixel efficacy region coordinate (x_{SRE}) [21] (and this is the absolute term). The x_{SRE} is the spatial coordinate where the intensity-curvature content admits an extreme [21] (i.e. the first order derivative is zero), thus where the signal-image intensity-curvature content change caused through re-sampling the signal-image is maximum or minimum. Therefore, the meaning of the intensity-curvature measure ICM(x) is that one of the ratio between the maximal (minimal) change of intensity-curvature content of the signal-image because of re-sampling, and the maximal (minimal) intensity-curvature content of the signal-image. The bivariate linear function h(x, y) is found in [1] and has equation:

$$h(x, y) = f(0,0) + x\theta_x + y\theta_y + xy\omega_f \qquad (25)$$

$$\theta_x = f(1,0) - f(0,0) \qquad (26)$$

$$\theta_y = f(0,1) - f(0,0) \qquad (27)$$

$$\omega_f = f(1,1) + f(0,0) - f(0,1) - f(1,0) \qquad (28)$$

where $f(0,1), f(1,0), f(1,1)$ are the values of the three pixels in the neighborhood of $f(0,0)$, which is the pixel being re-sampled. The

intensity-curvature functional $\Delta E(x, y)$ of Eq. (25) is found in [21] and is here reported after simplification:

$$\Delta E(x, y) = \frac{f(0,0)xy}{H_{xy}(x, y)} \qquad (29)$$

where $H_{xy}(x, y)$ is the primitive of h(x, y).

Results

The stack-based layering theory

This section opens up the presentation of the results with the application of the stack-based layering theory [25] to the MRI of the tumors in the human brain. Figs. 1–3 present to the reader the well known evidence that the tumor in the human brain develops across layers, and the figures show the direction and the form of the tumor propagation. The stack-based layering theory requires first the identification and the classification of the stack type. On the basis of Figs 1–3 and on the basis of Fig. 4, pg. 454 in [25], the stack types of the tumor MRI are multiple and they are indexed in [25] as S1$^+$ (above, top or upward), S2$^+$ (beneath, bottom or downward), S3$^+$ (single, double or all sided (external)), S4$^+$ (outward, outer or coating). Secondly, the stack-based layering theory requires analyzing how the tumors are formed layer after layer (slice after slice). The images provided in Fig. 1 show that the tumor is formed following a pattern of propagation that goes from slice 60 to 71 and depicts a shape that appears to be somehow circular at each slice consistently with the type of pathology as that one of the metastases. The pattern of propagation shown in Fig. 2 covers slices 21 through 10 and appears with various shapes at each slice, consistently with the type of pathology as that of one of the glioblastoma multiforme. Finally, the pattern of propagation seen in Fig. 3, where the intraventricular brain tumor is presented (see slices 17 through 6), shows matching of the pathology with the anatomy of the ventricles of the human brain, in other words the pathology attacks the ventricles and spreads into them, and also provokes a dilation of the ventricles. The histograms presented in Figs. 1–3 are an indication of the organization of the gray levels of the brain images. To conclude on the application of the stack-based layering theory it can be suggested that the flexibility of the Intensity-Curvature Measurement Approaches makes it feasible to apply the signal-image post-processing techniques to imaging of tumors on thyroid, liver, spleen and lymph nodes, and pancreas. The flexibility is warranted by the rigorous methodology based on calculus and algebra, which was employed to develop the Intensity-Curvature Measurement Approaches.

The Intensity-Curvature Measurement Approaches

In the following pictures (Figs. 4–15), in (a) is shown the collected MRI, whereas (b), (c), (d) and (e) show the classic-curvature (CC), the signal resilient to interpolation (SRI), the intensity-curvature measure (ICM) and the intensity-curvature functional (ICF) images respectively. Thus, each of the collected MRI reported in the result section is shown along with the four post-processed images in the quest for complementary and/or additional information. It will become clear in this section that in all of the three tumor cases presented in this

section, the signal resilient to interpolation (see Fig. 9 for instance), the classic-curvature (see Fig. 6 for instance) and the intensity-curvature functional (see Fig. 6 for instance) are those images which are capable of adding the most to the diagnosis made with the collected MRI.

In all of the results presented in this paper the wordings brightness-contrast enhanced and enhanced gray level intend to convey the meaning that the image had the contrast and the brightness changed. Naturally, the aforementioned wording is different from contrast enhancement through intravenous injection of the contrast agent.

In Fig. 4, both of the classic-curvature and the intensity-curvature functional (see (b) and (e)) show a *visually perceptible* third dimension perpendicular to the image plane and such dimension spans across the entire spatial extent of the brain pathology (metastases). The image in (d) which is the intensity-curvature measure shows the pathology in white, whereas the signal resilient to interpolation seen in (c) shows highlights of the pathology in three predominant different grayscale levels: white, dark and gray (see ellipse in (c)). The highlight of the pathology in three predominant different colors is consistent with the visualization shown in (a). The lesion tends to appear brighter (see white arrow in (a)) and consistently the pathology is imaged in darker color in (c) (see black arrow).

Additionally, in Fig. 4 in (c), the image provides with a well-behaved delineation of the tumor and the surrounding brain parenchyma. Also, in (c) is visible a well-behaved separation of the edema in its peripheral gray component and a well-behaved delineation of the central zone – solid part (dark central zone). In (d) is visible a well-behaved separation between the tumor and the surrounding brain parenchyma, only for what relates to the edema but not in the inner part of the tumor. In (b) and in (e) is visible a well-behaved medical intensity-curvature measure representation with well-behaved delineation of the brain architecture specifically of the brain gyri and sulci. Also (b) and (e) provide with a well-behaved anatomical localization of the brain constituent components, but without clear description of the lesion components.

Another interesting observation made through Fig. 4 is related to the *visually perceptible* third dimension provided with the classic-curvature and the intensity-curvature functional. When looking to (b) and to (e) inside the ellipse located to the left in (a) we distinguish two sulci and the Sylvian fissure. The declined sulcus is the one visible from the top, then the Sylvian fissure identifiable through the shape of 'τ', and another sulcus with the shape of 'z'. The aforementioned sulci and the Sylvian fissure are also visible in (c) and (d).

In Fig. 5, a remarkable observation that can be made on the basis of (b) and (e) when compared to (a) is the valley located at the center of the lesion which is imaged in gray (see arrow in (a) and compare to the arrow in (c) and (e)). The image in (c), which is the signal resilient to interpolation, offers three predominant grayscale colors which can be perceived when looking at the regions surrounding the area of the pathology indicated by the arrow. The three gray levels correspond to the coloring seen in (a) when looking at the pathology in the region surrounding the arrow. The appearance of the three predominant colors in (c) gives a more marked level of details of the pathology when compared to the image seen in (a). Also, in (c) is visible a well-behaved distinction between the brain parenchyma surrounding the tumor and the view of the constituent parts of the edema: (i) black outer zone, and (ii) the internal solid component (inner gray zone). In (d) is visible a well-behaved delineation of the whole difference between the brain parenchyma surrounding the tumor and the tumor itself, but without a clear view of the components of the tumor (i.e. no clear view of the inner solid segment). In (b) and in (e) is visible a well-behaved representation of the brain architecture, with a well-behaved identification of the anatomical structures and a well-behaved representation of the constituent components of the brain at different heights (the third dimension perpendicular to the imaging plane).

Generally, in Fig. 6, an observation which can be made while looking at the images in (a) (b) and (e), which are the collected MRI, the classic-curvature and the intensity-curvature functional respectively, is that the *visually perceptible* third dimension appears at the location of the pathology and also in the sulci of the human brain. Again the image in (c), which is the signal resilient to interpolation shows a predominant triplet of coloring in gray levels which corresponds to the three gray levels seen in (a) inside the ellipse. As far as (b) and (e) are concerned (classic-curvature and intensity-curvature functional images) the *visually perceptible* third dimension is observable at the location of both of the sulci and the pathology.

It can be reasoned that the process of merging the intensity with the curvature in the classic-curvature so as to obtain the intensity-curvature functional [1–3], or calculating the classic-curvature alone [1–3], is sufficient to determine a change in pixel intensity of the image and so to transform the change into a third dimension like appearance as visible in the images in (b) and in (e). It is due to emphasize on the novelty of the *visually perceptible* third dimension perpendicular to the image plane shown by the classic-curvature alone when re-sampling with the bivariate cubic polynomial [24]. This paper expands on results reported just recently in [24] confirming the novelty of the *visually perceptible* third dimension obtained when calculating the classic-curvature of the signal-image while fitting to the signal-image the bivariate cubic polynomial of Eq. (1). The difference versus previous works [24] is that in this manuscript is presented a detailed discussion of the results through the evaluation of each of the images resulting from the Intensity-Curvature Measurement Approaches. The discussion evaluates the content and the significance of each image with the purpose to seek for information which may be useful in human brain tumor MRI diagnostic settings. Thus, the overall novelty of the manuscript is that for the first time the images resulting from the post-processing techniques called Intensity-Curvature Measurement Approaches were evaluated qualitatively looking at the medical content for diagnostic purpose. Additionally, in Fig. 6 in (c) is visible a well-behaved delineation of the difference between the brain parenchyma surrounding the tumor and the tumor, and also re-imaging of the constituent parts of the edema (see gray outer zone) and the internal solid component (see inner black area). For what pertains to the anatomical localization, in (d) is visible a well-behaved and entire delineation of the changes of the human brain cortex because of the tumor, but not the components of the tumor. In (b) and in (e) is visible a well-behaved medical intensity-curvature measure representation of the human cortex, the anatomical localization of the tumor, and a well-behaved separation of the tumor from the surrounding parenchyma, but not a clear description of the individual components of the tumor.

In the image seen in (d) in Fig. 7, all of the brain structures are reproduced with the same level of details of the collected

MRI, however the image shown in (d) is brighter than the image shown in (a). The lesion structure is well observable in two tones: bright and dark. It can be argued however that the image seen in (d) is a fainted image of the original seen in (a). On the other hand, in (c) the signal resilient to interpolation shows three predominant gray levels in the region of the lesion: dark, strong gray and light gray. The images in (b) and (e), which are the classic-curvature and the intensity-curvature functional present the *visually perceptible* third dimension at the location of the lesion marked in white in (a). In (c) the image is useful as the inverted of (a) and shows well-behaved delineation of the details of the tumor (obtained because of the intravenous contrast agent), which are shown in dark-black. Also, in (c) the image shows well-behaved delineation of the inner zone of the tumor which is not enhanced through the contrast agent. The images in (e) and (b) are useful because they show the location of the tumor (imaged through the intravenous contrast agent) and because they emphasize on the incomplete margins of the tumor.

The next four pictures (Figs. 8–11) are concerned with the effects of a glioblastoma multiforme on the human brain. In Fig. 8, the *visually perceptible* third dimension appears accentuated in (b) versus (e) and the pathology appears to be located on a higher elevation with respect to the image plane. The images in (c) and in (d) show the pathology with two predominant gray levels in (c) and with a monotonic color which is white in (d). Inside the ellipses in (a), (b) and (c) are details that are accentuated in the post-processed images (see the two gray levels inside the ellipse in (c)). In (c) is visible a well-behaved separation between the tumor and the surrounding brain parenchyma, also a well-behaved visualization of the tumor marginal contours, and a well-behaved anatomical orientation. The image in (d) is similar to the image in (a) except for the brightness, and also reproduces the details of (a), but it contains less information. The images in (b) and in (e) allow a well-behaved medical intensity-curvature measure representation of the tumor in terms of the localization and in terms of the visualization of the marginal outline (contour), and also offer a well-behaved anatomical orientation.

The emphasis in Fig. 9a is on the following structures: (i) the core of the tumor, (ii) the tumor mass, both of them visible in the large ellipse; and (iii) the bright spots seen in the smaller ellipse. Fig. 9c shows the structures in inverted color with some advantages over what is shown in Fig. 9a. Fig. 9b and e shows a neat and distinguishable *visually perceptible* third dimension especially visible in the tumor mass, and finally Fig. 9d presents a flat image with the highlight of tumor mass in bright. Overall, the best benefit of the post-processed images remains in the signal resilient to interpolation (see Fig. 9c) where the visibility of the core of the tumor, the tumor mass, and the bright spots seen in the smaller ellipse is enhanced when compared to the collected MRI of Fig. 9a. Indeed, in (c) is shown a well-behaved representation of the tumor for what pertains to the visualization of its individual components, (i.e. well-behaved presentation of the tumor texture which is solid cystic and also well-behaved visualization of the surrounding edema). Also in (c) is shown a well-behaved presentation and visualization of the tumor affected brain white matter, which is presented as dark zones (see inside the ellipses), and a well-behaved presentation of the other brain structures localized in the hemisphere opposite to the tumor. Hence, the image in (c) provides useful information for the diagnosis. On the other hand, the image in (d) offers a fainted version of the original shown in (a), and so the information content is reduced. The images in (b) and in (e) show a well-behaved medical intensity-curvature measure representation of the tumor, however with a partial representation of the tumor constituents. The images in (b) and in (e) show also a well-behaved display of the edema, however there is reduced information content as far as regards the brain white matter (compare (b) and (e) in Fig. 6 with (b) and (e) in Fig. 9).

In Fig. 10a is discernible an agglomerate of three tumor structures each indicated by an arrow. A southwest structure in which the contour line is white (see lower arrow located to the left of the tumor structure), a northwest structure in which the contour line is white (see upper arrow located to the left of the tumor structure) and a central structure of gray color surrounded by the previously mentioned two structures (see lower arrow located at the right of the tumor structure).

The brightness-contrast enhancement in (c) of Fig. 10 is higher than that one discernible in (a), making it possible for the signal resilient to interpolation to be representative of the collected MRI. It is visible that the contour line of the three aforementioned structures is imaged in dark in (c) and also that the spatial extent of the central tumor mass is shown in bright in (c). Also, in (c) is visible a well-behaved representation of the tumor, a well-behaved distinction of the tumor from other anatomical structures. In the dark area of the tumor is visible an accumulation of the contrast agent which indicates the solid part. Also visible is a well-behaved display of the cystic part which is colored in white.

Additionally, in (b) and in (e) the tumor mass structure has a well-marked contour line shown by the *visually perceptible* third dimension in both of the pictures. In (b) and (e) is visible a well-behaved medical intensity-curvature measure representation of the tumor in terms of a well-behaved distinction of the tumor from the surrounding brain parenchyma, but no information is given of the individual components of the tumor (i.e. presumably because of accumulated contrast agent). The images in (b) and in (e) carry reduced amount of information (compare (b) and (e) in Fig. 6 with (b) and (e) in Fig. 10).

In (d), two levels of gray, one in white and the other one in gray, make the three tumor structures visible to the eye of the observer. However, the intensity-curvature measure is fainted versus the original image shown in (a), hence, (d) carries less information than the collected MRI.

Observations similar to those made in Fig. 10 are possible in Fig. 11 with the difference that in Fig. 11 there are two tumor masses well-defined and visible across the five images from (a) through (e) (see arrows). The signal resilient to interpolation seen in (c) shows the tumor masses surrounded by a dark contour line. And the same contour line is visible in (b) and in (e) with a neat and distinguishable *visually perceptible* third dimension, whereas in (d) the contour line is shown through a single white color and the tumor masses are shown through two different colors: white and gray. The *visually perceptible* third dimension is accentuated in (b) and in (e) at the margins of the tumor.

In (c) is visible a well-behaved representation of the tumor which is divided into two confluent parts; also, visible is a well-behaved distinction of the tumor from the surrounding parenchyma. The dark zone in (c) is accumulated contrast agent (which makes the coloring of the tumor in its solid part). Also,

in (c) is shown a well-behaved representation of the inner (cystic) part of the tumor, which is marked in white. The image in (d) does not provide any additional information to the image in (a). The images in (b) and in (e) show well-behaved medical intensity-curvature measure representation of the tumor in terms of distinction of the tumor from the surrounding brain parenchyma, but the images do not show the individual components of the tumor (i.e. presumably because of accumulated contrast agent). The images in (b) and in (e) carry reduced amount of information (compare (b) and (e) in Fig. 6 with (b) and (e) in Fig. 11).

Fig. 12b and Fig. 12c emphasize on the additional details provided through the classic-curvature (b) and the signal resilient to interpolation (c) for what is relevant to the cortex, the ventricles, and most importantly the intraventricular tumor. It is interesting to note that the gray level scale is more accentuated in the images shown in (b) and in (c) than it is in the collected MRI shown in (a) so as to give a finer level of details to the classic-curvature (b) and the signal resilient to interpolation (c) images. The Cerebrospinal Fluid (CSF) is shown in light gray in both (b) and (c), whereas (e) shows the *visually perceptible* third dimension all across the cortex, the spinal cord and the tumor mass.

In Fig. 12d, the intensity-curvature measure does not provide additional information to the image in (a). The appearance of the classic-curvature seen in (b) is remarkably different from what seen in Figs. 4b–11b and the reason of such change is the value of the parameter of the bivariate cubic Lagrange polynomial. In (e) the image provides with a well-behaved medical intensity-curvature measure representation of the tumor, and separation of the tumor from other anatomical structures. In (b) and in (c) is visible a well-behaved representation of the tumor and distinction of the tumor from the other anatomical structures of the brain, also a well-behaved anatomical orientation of the brain structures. Additionally, (b) and (c) offer the assessment of the tumor texture. In other words, (b) and (c) offer a well-behaved representation of the tumor with a good delineation of the tumor constituent components: both of the solid and the cystic parts. Finally, the image in (c) provides better information than the image in (b) because of the better contrast.

Unlike the images shown in Fig. 12b and Fig. 12c, the images shown in Fig. 13b and Fig. 13c present the same number of predominant colors highlighting the tumor mass inside the ventricle. The colors are white, black and gray and this is visible in both of the classic-curvature and the signal resilient to interpolation images of the tumor mass (see images in (b) and in (c) respectively). The image in (d), which is an intensity-curvature measure image, does not provide additional information versus the collected MRI shown in (a). The image in (e) provides with well-behaved medical intensity-curvature measure representation of the tumor but with partial level of details given that there is not clear distinction between the tumor and the space occupied by the Cerebrospinal Fluid (CSF). And the lack of clearness reduces the information content of the image. The images in (b) and in (c) provide with a well-behaved: representation of the tumor; distinction of the tumor from the surrounding structures; representation of the tumor constituent components, and representation of the CSF and the white matter. And finally, the images in (b) and in (c) show a well-behaved anatomical orientation, with the

image (b) bringing in more information than the image in (c) because of the better contrast.

In Fig. 14, when looking at the images in (b) and in (c) versus the collected MRI of (a) it is possible to make the following comparison. The tumor structures are well reproduced in (b) and in (c), see for example the white spots in (a) (visible at the center of the tumor mass) and the corresponding black spots in (b) and in (c), and also the spatial extent of the tumor visible in all of (a), (b) and (c). The structure of the tumor as shown in (a) is pervading the ventricle as indicated in the three images by the arrow and such structure is colored in white in (b) and in (c). Similar to (a), (b) and (c), in (d) and in (e) the tumor mass is pervading the healthy tissue located in between the two ventricles and this is shown inside the ellipses (see (d) and (e)). The image in (e) shows well-behaved medical intensity-curvature measure representation of the tumor with partial level of details (i.e. there is not entirely clear distinction between the CSF and the tumor because of the location of the tumor), and this aspect reduces the information content of the image. The images in (b) and in (c) offer well-behaved: representation of the tumor; distinction between the tumor and the surrounding structures; representation of the tumor constituent components; representation of the CSF and the brain white matter; and anatomical orientation. Finally, the image in (c) conveys more information than the image in (b). The image in (d) does not provide additional information to the image seen in (a).

In general, we can see that in Fig. 15 the images in (b) and in (c) are complementary to the collected MRI in (a). As far as regards the images in (d) and in (e), they provide with additional evidence that the healthy tissue in between the ventricles appears deeply affected by the tumor mass. As in Fig. 14, the image in (e) offers a well-behaved medical intensity-curvature measure representation of the tumor with partial level of details, because of the location of the tumor. The tumor does not allow entire and clear visualization of the CSF and so the information content of the image in (e) is reduced. In (b) and in (c), the images offer well-behaved: visualization of the whole tumor; representation of the CSF (in both left and right ventricles); representation of the blood vessels around the tumor; and anatomical orientation. The intensity-curvature measure shown in (d) does not offer additional information to (a).

Statistical analysis

The Kolmogorov–Smirnov test was employed to ascertain as to whether the frequency histograms of the classic-curvature and the intensity-curvature functional were normally distributed. The Kolmogorov–Smirnov test was performed in the cases presented in Figs. 4–15 and it has been found that the classic-curvature and the intensity-curvature functional histograms are not normally distributed (alpha = 0.01) although presenting Gaussian like shape as shown in Figs. 4–15. Both of the values of D_n (result of the test) and D (critical value) are reported in the figure captions ($D_n < D$ implies the Gaussian distribution). The histograms throughout the manuscript show along the abscissa the pixel intensity value scaled in the range $[0, 255]$, and along the ordinate the number of times the pixel intensity value is found in the image.

Discussion

The literature

The combination of Magnetic Resonance Spectroscopy (MRS) with T1-weighted MRI provides with a powerful diagnostic tool. Specifically, MRS yields additional information to the one available through MRI [26]. One complication might be in the low intensity signals of MRS, however, the concurrent usage of MRS, MRI, and dynamic nuclear polarization (DNP) has been reported to have overcome such barrier [27]. The use of MRS in tumor diagnosis intends to locate healthy tissues and tumor tissues through the injection of one specific compound which acts as a trigger to enhance the presence of some metabolites which behavior is that one of the tumor specific marker [28]. More specifically MRS is capable of identifying tumor regions and distinguishing them from healthy regions on the basis of the response offered by the metabolites behavior (N-acetyl aspartate (NAA), for instance [29] or choline [30]), regardless of the injection of a compound and the observation of the subsequent metabolism.

Proton spectroscopic imaging used together with perfusion weighted MRI (PWI) has been reported to be successful in diagnostic settings when trying to distinguish between two types of brain tumor pathologies: metastases and gliomas [30]. The aforementioned study aimed to demonstrate the feasibility of additional data collection (physiologic and metabolic information in addition to T1-weighted MRI) from the peritumoral region with MRS and also to confirm that the peritumoral region differs from healthy white matter, and such confirmation was achieved through measurements of the choline-to-creatine ratio [30]. The Intensity-Curvature Measurement Approaches presented and employed in our research allow though full disclosure of information related to the tumor from the entire MRI images, thus it is possible to see the effect of the post-processing in the peritumoral region too.

Diffusion Weighted Imaging (DWI) and Diffusion Tensor Imaging (DTI) have been used together to identify tumor components, and to see the difference between tumor and normal brain tissue or edema [31]. Thus, another technique that may prove successful in providing additional information to the classic T1-weighted MRI is Diffusion Weighted MRI (DWI). Indeed DWI is capable of providing the diagnostic settings with the information relevant to the water diffusion and propagation, and so the information relevant to the viability of the tissues in the human brain [32]. DWI is thus capable of measuring the anisotropic molecular motion within the brain [32]. In addition to the capabilities offered to the diagnosis through the combination of DWI and MRI is the Diffusion Tensor Imaging (DTI) technique, which can add additional evidence (to the evidence offered by DWI alone) of the evolution of the brain disease [31], through the property of some unhealthy tissue to display obstruction to water propagation in the human brain. DTI is thus a DWI technique and is mainly computational as it provides the diagnostic settings through the diffusion tensor of the magnitude, the degree of anisotropy, and the orientation of diffusion anisotropy [32–34].

The visually perceptible third dimension

The novelty in the concept of the third dimension needs to be thought of as the third dimension *visually perceptible* along the axis perpendicular to the imaging plane. As previous work done on human brain tumors detected through MRI shows, the *visually perceptible* third dimension appears when the intensity-curvature functional is calculated from the bivariate linear function [1]. In this paper is shown that the third dimension is *visually perceptible* also when calculating the classic-curvature from the bivariate cubic polynomial. Fig. 16 shows a comparison of the classic-curvature (see (e)) and the intensity-curvature functional (see (f)), with the high pass filter mask shown in (g), and reveals that the calculation of both of the aforementioned Intensity-Curvature Measurement Approaches is similar to the calculation of the filter mask. The novelty introduced by the two aforementioned Intensity-Curvature Measurement Approaches consists in the math formulation which making use of calculus and algebra reproduces the effect of the high pass filter.

The relationship between MRI signal processing and the proposed aim

A short review of the literature in MRI signal-image processing of the human brain is in order to explain one of the proposed aims of this paper. Normally, the first step of MRI post-processing of the human brain is segmentation [35]. If the MRI data are collected multiple times, for instance to monitor the progression (regression) of a disease, a common signal processing technique is registration [36], which is conducted in order to map MRI multiple collections on a voxel-by-voxel basis. Additionally, if MRI is to be analyzed together with another imaging modality like Computerized Tomography and/or functional MRI, the signal-image processing technique required is co-registration [37,38]. Moreover, after the MRI data has been segmented and registered, depending on the aim of the post-processing of the original signal, filtering is performed in order to highlight the features of interest of the MRI signal-image [39]. The Intensity-Curvature Measurement Approaches presented in this paper are post-processing techniques which do not require segmentation, indeed they can also be employed after registration and/or co-registration of imaging modalities, and also they do not require filtering of the signal-image. Magnetic Resonance Imaging (MRI) of the human brain [40,41] can attain additional and/or complementary information about the case under study from a variety of techniques all derived from MRI as well as other techniques like Computerized Tomography (CT) [42], Positron Emission Tomography (PET) [43] and Single-Photon Emission Computed Tomography (SPECT) [44]. Among others, the MRI techniques are: (i) T1-weighted contrast enhanced MRI [45], (ii) T2-weighted MRI [46], (iii) Perfusion Weighted Imaging (PWI) [47], (iv) Diffusion Weighted Imaging (DWI) [48], (v) Diffusion Tensor Imaging (DTI) [49], (vi) Susceptibility Weighted Imaging (SWI) [50], (vii) Magnetic Resonance Spectroscopy (MRS) [51,52], (viii) Magnetic resonance angiography (MRA) (including FLASH MRI and Magnetic resonance venography) [51], (ix) Functional MRI (fMRI) [53], (x) intraoperative MRI [54], (xi) Magnetic resonance guided focused ultrasound [55], (xii) Multinuclear imaging

[56], (xiii) Molecular imaging by MRI [57]. Current state of the art in neuroimaging offers also techniques like (xiv) Magneto-enchephalography (MEG) and Electroencephalography (EEG) [58], in which results are advocated through the imaging capability of MRI.

The reason as to why the Intensity-Curvature Measures are used as post-processing methodologies of the MRI of the human brain is for capturing complementary and/or additional information not readily visible through T1-weighted MRI. For instance, Fig. 16b is a clear demonstration of the capability of the signal resilient to interpolation to add information to the T1-weighted MRI, because the SRI highlights human brain features through the modification (illumination) of the signal-image. As it can be seen in the image in Fig. 16b, the illumination consists in an enhancement of the contrast which makes easier the capturing details of the MRI image seen in Fig. 16a.

The significance of the Intensity-Curvature Measurement Approaches

The research presented in this paper makes use of post-processed MRI images in order to collect information useful in MRI diagnostic settings. To establish a link with the goals of the study and to stress on the relevance of the results to the MRI diagnostic settings, some remarks are for what pertains to the significance and therefore the diagnostic value of the images collected through the Intensity-Curvature Measurement Approaches.

On the basis of the information collected in Figs. 4–9 we can summarize that the significance of the signal resilient to interpolation (shown in (c) of each figure) is to demarcate the tumor structures as clearly as the collected MRI and this happens with a stretched gray level scale. The signal resilient to interpolation is thus able to add information to the diagnosis. On the other hand the significance of the classic-curvature (b), the intensity-curvature measure (d) and the intensity-curvature functional (e) is to add: (i) complementary information when showing the tumor contour line, and (ii) additional information when showing the *visually perceptible* third dimension of tumor structure on the imaging plane (see (b) and (e) of each figure).

More specifically, in Fig. 4c, the signal resilient to interpolation provides with delineation of the tumor and separation of the tumor from the healthy tissues.

Fig. 5c, which is also a signal resilient to interpolation image, shows clearly the constituent parts of the edema, whereas Figs. 5b and 5e show the architecture of the human brain.

Fig. 6d, which is an intensity-curvature measure, shows the transformation of the human brain because of the tumor, along with a well-defined localization of the tumor. Figs. 6b and 6e, which are the classic-curvature and the intensity-curvature functional respectively, show a non-indifferent number of features: (i) medical intensity-curvature measure representation of the human cortex, (ii) anatomical localization of the tumor, (iii) separation of the tumor from the surrounding parenchyma, however (iv) not a clear description of the individual components of the tumor.

Moreover, Fig. 6c, which is a signal resilient to interpolation image, provides with clear distinction between the tumor and the surrounding parenchyma and clear distinction of the

tumor components: (i) edema, and (ii) internal solid component.

Figs. 7b and 7e, which are the classic-curvature and the intensity-curvature functional respectively, emphasize on the lack of tumor contour line.

Fig. 8c, which is a signal resilient to interpolation image, shows separation between the tumor and the surrounding brain parenchyma.

Fig. 9c, which is a signal resilient to interpolation image, shows the texture of the tumor and the surroundings of the edema along with a clear visualization of the brain white matter affected by the tumor. We find Fig. 9c the most useful for a diagnosis among the images herein presented.

What can be seen from Figs. 10 and 11 is that the contour line in (c) matches with the contour line in (a) and also with the *visually perceptible* third dimension in (b) and in (e), suggesting that there might be fluids (due to the accumulation of contrast agent) at the location of the contour line (see (a)) and such fluids are shown in (b) and in (e) and also with dark color in (c) (see (c) versus white in (a)). More specifically, Fig. 10c, which is a signal resilient to interpolation image, shows an accumulation of the contrast agent at the location highlighted in dark, which localizes the solid part of the tumor, and the cystic part which is colored in white.

Likewise Fig. 10c, Fig. 11c (both of them signal resilient to interpolation images) show the distinction of the tumor mass into two different colored parts: (i) dark (solid part indicated through the accumulation contrast agent) and (ii) white (cystic part of the tumor). As Fig. 11, the images in (b) and in (e), which are classic-curvature and intensity-curvature functional images respectively, show a well-structured localization of the tumor and a clear separation of the tumor from the surrounding parenchyma.

All of the images shown in Fig. 12 were brightness-contrast enhanced, and the difference between the gray matter and the white matter fibers of the brain is accentuated in (b) and in (c). Also, (b) and (c) show the tumor in two main gray levels. One is dark and it shows the center of the tumor and one is gray and it shows the outer surface as well as the structure of the fibers of the pathology. Such level of details is well marked in (b) and in (c) versus the collected MRI shown in (a). Given the appearance of (b) and (c), if there was an anomaly in the cortex and more specifically within the white matter fiber tracks, it would be easier to note in the classic-curvature and signal resilient to interpolation images. And so, the significance of the classic-curvature and the signal resilient to interpolation in Fig. 12 is to add diagnostic value. Additionally, texture, well-defined representation of the two parts of the tumor (solid and cystic) and anatomical orientation of the brain structures are the three main features offered by the images in Fig. 12b and 12c, which are classic-curvature and signal resilient to interpolation images respectively.

In Fig. 13, the intensity-curvature measure in (d) depicts the anatomy very much like the collected MRI, and the intensity-curvature functional in (e) offers the *visually perceptible* third dimension to the entire cortical structure and the borderline of the ventricles which include a region where both the CSF and the tumor mass are imaged. The significance of the images in (b) and in (c) is that they present an alternative vision (to the MRI shown in (a)) of both the brain and the tumor but with different grayscale level and also different shading. Again in

Figs. 13b and 13c, the classic-curvature and the signal resilient to interpolation images respectively show a clear representation of: (i) the tumor in its whole, and (ii) the tumor in its components. The tumor is also visualized as distinct from the surrounding structures; the CSF and the white matter are well represented. Moreover, the images show clear anatomical orientation.

In Fig. 14, the region of the tumor attached to the intraventricular tissue is well represented in (b), (c), (d) and (e). Indeed as it is visible in (e) the tumor mass has destroyed the intraventricular tissue which separates the right ventricle from the left ventricle. Fig. 15 allows observations similar to those already made while commenting Fig. 14. The observations made when looking at Figs. 14 and 15 make it possible to discern the significance of the intensity-curvature functional in (e) which is that one of providing information useful to the diagnosis.

Fig. 14e, which is an intensity-curvature functional image, shows a non-distinct localization of the tumor because of the mixture of the tumor with the CSF, whereas the observations made in Fig. 13b and 13c, which convey information useful to the diagnosis, also apply to Fig. 14b, Fig. 15b (classic-curvature images) and Fig 14c and Fig. 15c (signal resilient to interpolation images).

Due to the originality of this research it is not possible to make comparisons with results offered by other studies. The information provided to the collected MRI by the Intensity-Curvature Measurement Approaches, utilized in order to post-process the data, highlights on the significance of: (i) the signal resilient to interpolation to offer additional details, and (ii) the classic-curvature together with the intensity-curvature functional to offer the *visually perceptible* third dimension perpendicular to the imaging plane. The information is useful in diagnostic settings and acts as if the MRI is observed using different visual instruments which are capable of highlighting features not readily observable in the original images.

On the interpretation of the results

The Intensity-Curvature Measurement Approaches are images derived from the collected MRI and such images are already a consequence of mathematical analysis. Nevertheless, we think that one fair and straightforward way to communicate the meaning of the Intensity-Curvature Measurement Approaches is to display the images and to have them analyzed by radiologists, whom write about the qualitative content under a medical perspective. Therefore, what is reported in the paper is the medical qualitative content of the Intensity-Curvature Measurement Approaches. The aforementioned analysis has the advantage to raise a debate about the medical content of the Intensity-Curvature Measurement Approaches and also the disadvantage of making the analysis subjective to the radiologist's opinion. Thus, the interpretation can be somehow subjective to the radiologist point of view, but it is the radiologist integrity and experience that makes the interpretation logical and legitimate. Moreover, the terminology: ' medical intensity-curvature measure representation of the human cortex' is new and is included in this manuscript so to make it easier and simplified the understanding of the images which show the *visually perceptible* third dimension. In other words, 'a medical intensity-curvature measure map' of the brain parenchyma, is a terminology which relates to the characteris-

tics of the aforementioned images. The characteristics of the images provide, through the *visually perceptible* third dimension, with the identification of the difference between the edema and the rest of brain parenchyma.

The scientific contribution

The scientific contribution of our research consists in the introduction into the scientific literature of signal-image post-processing techniques which are called in this paper Intensity-Curvature Measurement Approaches and the math of such post-processing techniques is reported in the section titled: 'The mathematical formulation'. The scientific contribution is warranted by the rigorous methodology based on calculus and algebra employed to invent the Intensity-Curvature Measurement Approaches and so by the presentation of novel imaging methodologies called: (i) classic-curvature, (ii) intensity-curvature functional, (iii) signal resilient to interpolation, and (iv) intensity-curvature measure. The scientific contribution bases its root foundations into two main concepts. The first concept is the math engineering tool called intensity-curvature functional, which, in an image, combines together both of the intensity and the curvature (second order derivative of the signal-image) into a single parameter. The second concept is the true and rigorous methodology adopted in order to calculate first and second order derivatives of the signal-image. Additionally, the scientific contribution is warranted by the signal resilient to interpolation. The signal resilient to interpolation is the signal derived from an original signal-image, falsifying the assumption of equality between non re-sampled signal-image and re-sampled signal-image. This paper reports on results obtainable through the signal resilient to interpolation when applied to human brain tumors detected through MRI. See Fig. 16b to appreciate the potentials of the signal resilient to interpolation. Finally, the other Intensity-Curvature Measurement Approach called intensity-curvature measure also adds scientific contribution because of the aforementioned two concepts. The methodology used to calculate the second order derivatives of a signal-image clearly departs from methodologies like the Sobel operator and/or the gradient.

The main findings

The main findings of this research are: (i) the signal resilient to interpolation provides the MRI with an enhanced gray scale, and (ii) the classic-curvature and the intensity-curvature functional show the capability to extract a *visually perceptible* third dimension from 2D MRI images. In support to the aforementioned findings eight additional human brain tumor MRI cases were studied and the results are shown in Figs. 17–19. The histograms are not presented because the three figures are focused on the main findings. Figs. 17a and 17b show the contrast enhanced T1-weighted MRI and the signal resilient to interpolation respectively. Worth of note is the enhanced level of details shown in Figs. 17b versus 17a (see inside the white ellipses). The MRI shown in 17a, 17c, 17e, 17g and 17i, have not been contrast enhanced though. Figs. 17c and 17d show the collected FLAIR MRI and the classic-curvature calculated with the bivariate cubic polynomial. See the tumor inside the ellipse in (c) and the corresponding *visually perceptible* third

dimension shown in (d) inside the ellipse, which appears elevated when looking at the ventricles and appears however at the same height of the brain sulci. Additional confirmation of the enhancement of the grayscale level versus the T1-weighted MRI is provided in Fig. 17f where is shown the signal resilient to interpolation of Fig. 17e (contrast enhanced T1-weighted MRI). The intensity-curvature functional of Fig. 17h is calculated using the bivariate linear function to process the contrast enhanced T1-weighted MRI shown in Fig. 17g, and shows the tumor contour line as well the *visually perceptible* third dimension in those regions which are seen in bright color in Fig. 17g. In Fig. 17j is shown the signal resilient to interpolation of the contrast enhanced T1-weighted MRI, which is shown in Fig. 17i, and it is confirmed the enhanced grayscale level as well as illumination of the region inside the ellipse where is visible the tumor spreading into the ventricle. Fig. 18 shows a T2-weighted MRI in (a) and the intensity-curvature functional calculated with the bivariate linear function in (b). Worth of note is the *visually perceptible* third dimension shown in (b) (see regions of the image pointed by the arrow), which corresponds to the regions of the edema seen in (a). Fig. 18d shows a *visually perceptible* third dimension (see inside the ellipse) which corresponds to the bright spots (pathology) seen in Fig. 18c (contrast enhanced T1-weighted MRI) inside the ellipse. Fig. 19a shows a FLAIR MRI and Fig. 19b shows the intensity-curvature functional with the *visually perceptible* third dimension in the region of the edema indicated by the arrow. The intensity-curvature functional images seen in Figs. 18d and 19b were calculated when using the bivariate linear function.

Conclusions

On the basis of the math developed in [21,22], computer programs that calculate the four Intensity-Curvature Measurement Approaches have been written and used to obtain the results presented in this manuscript. Thus, replication of the results is certain as well is certain the availability to employ the computer programs in other real life cases in medical settings with applications not limited to human brain tumors detected through MRI. This article provides with results obtained with the four post-processing techniques called Intensity-Curvature Measurement Approaches and the results are useful to aid the diagnosis of tumors in the human brain detected through MRI. The human brain MRI images have been analyzed concurrently with the Intensity-Curvature Measurement Approaches. The Intensity-Curvature Measurement Approaches are: (i) classic-curvature, (ii) signal resilient to interpolation, (iii) intensity-curvature measure and (iv) intensity-curvature functional. The signal resilient to interpolation has been shown to provide the MRI with an enhanced gray scale. Also, the results presented in this paper confirm the capability of both of the classic-curvature and the intensity-curvature functional to extract the *visually perceptible* third dimension from 2D MRI images.

Conflict of Interest

The authors have declared no conflict of interest.

References

[1] Ciulla C, Rechkoska Shikoska U, Capeska Bogatinoska D, Risteski FA, Veljanovski D. On the intensity-curvature functional of the bivariate linear function: the third dimension of magnetic resonance 2D images in a tumor case study. Am J Signal Process 2014;4:41–8.

[2] Ciulla C, Capeska Bogatinoska D, Risteski FA, Veljanovski D. Computational intelligence in magnetic resonance imaging of the human brain: the classic-curvature and the intensity-curvature functional in a tumor case study. Int J Inf Eng Electron Business 2014;6:1–8.

[3] Ciulla C, Capeska Bogatinoska D, Risteski FA, Veljanovski D. Applied computational engineering in magnetic resonance imaging: a tumor case study. Int J Image Graphics Signal Process 2014;6:1–9.

[4] Cha S. Update on brain tumor imaging: from anatomy to physiology. Am J Neuroradiol 2006;27:475–87.

[5] Al-Okaili, Riyadh N, Krejza J, Wang S, Woo JH, Melhem ER. Advanced MR imaging techniques in the diagnosis of intra-axial brain tumors in adults. Radiographics 2006;26:S173–89.

[6] Chao ST, Suh JH, Raja S, Lee S-Y, Barnett G. The sensitivity and specificity of FDG PET in distinguishing recurrent brain tumor from radionecrosis in patients treated with stereotactic radiosurgery. Int J Cancer 2001;96:191–7.

[7] Dashjamts T, Yoshiura T, Hiwatashi A, Yamashita K, Abe K, Ohyagi Y, et al. Asymmetrical cerebral perfusion demonstrated by noninvasive arterial spin-labeling perfusion imaging in a patient with corticobasal degeneration. Jpn J Radiol 2010;28:75–8.

[8] Lydie ND, Herlidou S, De Marco G, Gondry-Jouet C, Le Gars D, Deramond H, et al. Differential MRI diagnosis between brain abscesses and necrotic or cystic brain tumors using the apparent diffusion coefficient and normalized diffusion-weighted images. Magn Reson Imaging 2003;21:645–50.

[9] Dirk P, Floeth F, Hamacher K, Riemenschneider MJ, Reifenberger G, Müller H-W, et al. O-(2-[18F] fluoroethyl)-L-tyrosine PET combined with MRI improves the diagnostic assessment of cerebral gliomas. Brain 2005;128:678–87.

[10] Hori M, Ishigame K, Kabasawa H, Kumagai H, Ikenaga S, Shiraga N, et al. Precontrast and postcontrast susceptibility-weighted imaging in the assessment of intracranial brain neoplasms at 1.5 T. Jpn J Radiol 2010;28:299–304.

[11] Isobe T, Yamamoto T, Akutsu H, Anno I, Shiigai M, Zaboronok A, et al. Proton magnetic resonance spectroscopy findings of hemangioblastoma. Jpn J Radiol 2010;28:318–21.

[12] Kinoshita Y, Yokota A. Absolute concentrations of metabolites in the human brain tumors using in vitro proton magnetic resonance spectroscopy. NMR Biomed 1997;10:2–12.

[13] Preul MC, Caramanos Z, Collins DL, Villemure J-G, Leblanc R, Olivier A, et al. Accurate, noninvasive diagnosis of human brain tumors by using proton magnetic resonance spectroscopy. Nat Med 1996;2:323–5.

[14] Zacharaki EI, Wang S, Chawla S, Soo Yoo D, Wolf R, Melhem ER, et al. Classification of brain tumor type and grade using

MRI texture and shape in a machine learning scheme. Magn Reson Med 2009;62:1609–18.

[15] Schellinger PD, Meinck HM, Thron A. Diagnostic accuracy of MRI compared to CCT in patients with brain metastases. J Neurooncol 1999;44:275–81.

[16] Shih-Chin C, Lai P-H, Chen W-L, Weng H-H, Ho J-T, Wang J-S, et al. Diffusion-weighted MRI features of brain abscess and cystic or necrotic brain tumors: comparison with conventional MRI. Clin Imaging 2002;4:227–36.

[17] Goehde SC, Hunold P, Vogt FM, Ajaj W, Goyen M, Herborn CU, et al. Full-body cardiovascular and tumor MRI for early detection of disease: feasibility and initial experience in 298 subjects. Am J Roentgenol 2005;184:598–611.

[18] Singh SK, Hawkins C, Clarke ID, Squire JA, Bayani J, Hide T, et al. Identification of human brain tumor initiating cells. Nature 2004;432:396–401.

[19] Sugahara T, Korogi Y, Kochi M, Ikushima I, Shigematu Y, Hirai T, et al. Usefulness of diffusion-weighted MRI with echo-planar technique in the evaluation of cellularity in gliomas. J Magn Reson Imaging 1999;9:53–60.

[20] Saleem SN, Fetal MRI. An approach to practice: a review. J Adv Res 2014;5:507–23.

[21] Ciulla C. Improved signal and image interpolation in biomedical applications: the case of magnetic resonance imaging (MRI). Medical information science reference. IGI Global Publisher; 2009.

[22] Ciulla C. Signal resilient to interpolation: an exploration on the approximation properties of the mathematical functions. CreateSpace Publisher; 2012.

[23] Dooley SR, Nandi AK. Notes on the interpolation of discrete periodic signals using sinc function related approaches. IEEE Trans Signal Process 2000;48:1201–3.

[24] Ciulla C, Rechkoska Shikoska U, Capeska Bogatinoska D, Risteski FA, Veljanovski D, Madevska Bogdanova A, et al., editors. Biomedical image processing of magnetic resonance imaging of the pathological human brain: an intensity-curvature based approach. Ohrid, Republic of Macedonia: ICT Innovations; 2014. p. 56–65.

[25] Dorrah HT. Consolidity: stack-based systems change pathway theory elaborated. Elsevier Ain Shams Eng J 2014;5:449–73.

[26] Simonetti AW, Melssen WJ, van der Graaf M, Postman GJ, Heerschap A, Buydens LM. A chemometric approach for brain tumor classification using magnetic resonance imaging and spectroscopy. Anal Chem 2003;75:5352–61.

[27] Golman K, Ardenkjaer-Larsen JH, Petersson JS, Mansson S, Leunbach I. Molecular imaging with endogenous substances. Proc Natl Acad Sci USA 2003;100:10435–9.

[28] Golman K, Zandt R, Lerche M, Pehrson R, Ardenkjaer-Larsen J-H. Metabolic imaging by hyperpolarized ^{13}C magnetic resonance imaging for in vivo tumor diagnosis. Cancer Res 2006;66:10855–60.

[29] Dowling C, Bollen AW, Noworolski SM, McDermott MW, Barbaro NM, Day MR, et al. Preoperative proton MR spectroscopic imaging of brain tumors: correlation with histopathologic analysis of resection specimens. Am J Neuroradiol 2001;22:604–12.

[30] Law M, Cha S, Knopp EA, Johnson G, Arnett J, Litt AW. High-grade gliomas and solitary metastases: differentiation by using perfusion and proton spectroscopic MR imaging. Radiology 2002;222:715–21.

[31] Sundgren PC, Dong Q, Gómez-Hassan D, Mukherji SK, Maly P, Welsh R. Diffusion tensor imaging of the brain: review of clinical applications. Neuroradiology 2004;46:339–50.

[32] Schaefer PW, Grant PE, Gonzalez RG. Diffusion-weighted MR imaging of the brain. Radiology 2000;217:331–45.

[33] Sotak CH. The role of diffusion tensor imaging in the evaluation of ischemic brain injury – a review. NMR Biomed 2002;15:561–9.

[34] Alexander AL, Lee JE, Lazar M, Field AS. Diffusion tensor imaging of the brain. Neurotherapeutics 2007;4:316–29.

[35] Zhang Y, Brady M, Smith S. Segmentation of brain MR images through a hidden Markov random field model and the expectation maximization algorithm. IEEE Trans Med Imaging 2001;20:45–57.

[36] Arno K, Andersson J, Ardekani BA, Ashburner J, Avants B, Chiang M-C, et al. Evaluation of 14 nonlinear deformation algorithms applied to human brain MRI registration. NeuroImage 2009;46:786–802.

[37] Daisne J-F, Sibomana M, Bol A, Cosnard G, Lonneux M, Grégoire V. Evaluation of a multimodality image (CT, MRI and PET) coregistration procedure on phantom and head and neck cancer patients: accuracy, reproducibility and consistency. Radiother Oncol 2003;69:237–45.

[38] Andreas G, Geissler A, Foki T, Tahamtan AR, Pahs G, Barth M, et al. Comparison of fMRI coregistration results between human experts and software solutions in patients and healthy subjects. Eur Radiol 2007;17:1634–43.

[39] Gerig G, Kubler O, Kikinis R, Jolesz FA. Nonlinear anisotropic filtering of MRI data. IEEE Trans Med Imaging 1992;11:221–32.

[40] Lauterbur PC. Image formation by induced local interactions: examples of employing nuclear magnetic resonance. Nature 1973;242:190–1.

[41] Mansfield P. Proton magnetic resonance relaxation in solids by transient methods. PhD thesis. Queen Mary College, University of London; 1962.

[42] Davis KR, Ackerman RH, Kistler JP, Mohr JP. Computed tomography of cerebral infarction: hemorrhagic, contrast enhancement, and time of appearance. Comput Tomogr 1977;1:71–86.

[43] Raichle ME. Positron-emission tomography. Brain Metastasis 1980;2:246–53, Springer, Netherlands.

[44] Halama JR, Henkin RE. Single photon emission computed tomography (SPECT). Freeman and Johnson's Clin Radionuclide Imaging 1986;3.

[45] Tofts PS, Brix G, Buckley DL, Evelhoch JL, Henderson E, Knopp MV, et al. Estimating kinetic parameters from dynamic contrast-enhanced T1-weighted MRI of a diffusable tracer: standardized quantities and symbols. J Magn Reson Imaging 1999;10:223–32.

[46] Moseley ME, Cohen Y, Mintorovitch J, Chileuitt L, Shimizu H, Kucharczyk J, et al. Early detection of regional cerebral ischemia in cats: comparison of diffusion- and T2-weighted MRI and spectroscopy. Magn Reson Med 1990;14:330–46.

[47] Cutrer F, Michael A, Sorensen G, Weisskoff RM, Østergaard L, Del Rio MS, et al. Perfusion weighted imaging defects during spontaneous migrainous aura. Ann Neurol 1998;43:25–31.

[48] Le Bihan D, Breton E, Lallemand D, Grenier P, Cabanis E, Laval-Jeantet M. MR imaging of intravoxel incoherent motions: application to diffusion and perfusion in neurologic disorders. Radiology 1986;161:401–7.

[49] Pierpaoli C, Jezzard P, Basser PJ, Barnett A, Di Chiro G. Diffusion tensor MR imaging of the human brain. Radiology 1996;201:637–48.

[50] Haacke EM, Xu Y, Cheng YCN, Reichenbach JR. Susceptibility weighted imaging (SWI). Magn Reson Med 2004;52:612–8.

[51] Haacke EM, Brown RF, Thompson M, Venkatesan R. Magnetic resonance imaging: physical principles and sequence design. New York: J. Wiley & Sons; 1999.

[52] Golder W. Magnetic resonance spectroscopy in clinical oncology. Onkologie 2004;27:304–9.

[53] Ogawa S, Menon RS, Tank DW, Kim S-G, Merkle H, Ellermann JM, et al. Functional brain mapping by blood oxygenation level-dependent contrast magnetic resonance

imaging. A comparison of signal characteristics with a biophysical model. Biophys Soc 1993;64:803–12.

[54] Nimsky C, Ganslandt O, Buchfelder M, Fahlbusch R. Intraoperative visualization for resection of gliomas: the role of functional neuronavigation and intraoperative 1.5 T MRI. Neurol Res 2006;28:482–7.

[55] Cline HE, Schenck JF, Hynynen K, Watkins RD, Souza SP, Jolesz FA. MR-guided focused ultrasound surgery. J Comput Assist Tomogr 1992;16:956–65.

[56] Lysova AA, Koptyug IV, Sagdeev RZ, Parmon VN, Bergwerff JA, Weckhuysen BM. Noninvasive in situ visualization of supported catalyst preparations using multinuclear magnetic resonance imaging. J Am Chem Soc 2005;127:11916–7.

[57] Flacke S, Fischer S, Scott MJ, Fuhrhop RJ, Allen JS, McLean M, et al. Novel MRI contrast agent for molecular imaging of fibrin implications for detecting vulnerable plaques. Circ J Am Heart Assoc 2001;104:1280–5.

[58] Darvas F, Pantazis D, Kucukaltun-Yildirim E, Leahy RM. Mapping human brain function with MEG and EEG: methods and validation. NeuroImage 2004;23:S289–99.